(*c*) the diffraction intensity $|\Phi(U)|^2$ is a radially symmetric, smoothly varying function such as is normally produced by a sufficiently large area of the image of an amorphous material;

(*d*) there is no astigmatism present and no drift of the specimen; either of these factors would remove the radial symmetry.

From the form of (2.5.2.54) and a preknowledge of $|\Phi(U)|^2$, the zero crossings of $\sin\chi$ and the form of $E(U)$ may be deduced. Analysis of a through-focus series of images provides more complete and reliable information.

(2) Detail on a scale much smaller than the resolution of the electron microscope, as defined above, is commonly seen in electron micrographs, especially for crystalline samples. For example, lattice fringes, having the periodicity of the crystal lattice planes, with spacings as small as 0.6 Å in one direction, have been observed using a microscope having a resolution of about 2.5 Å (Matsuda *et al.*, 1978), and two-dimensionally periodic images showing detail on the scale of 0.5 to 1 Å have been observed with a similar microscope (Hashimoto *et al.*, 1977).

Such observations are possible because

(*a*) for periodic objects the diffraction amplitude $\Psi_0(uv)$ in (2.5.2.31) is a set of delta functions which may be multiplied by the corresponding values of the transfer function that will allow strong interference effects between the diffracted beams and the zero beam, or between different diffracted beams;

(*b*) the envelope functions for the WPOA, arising from incoherent imaging effects, do not apply for strongly scattering crystals; the more general expression (2.5.2.36) provides that the incoherent imaging factors will have much less effect on the interference of some sets of diffracted beams.

The observation of finely spaced lattice fringes provides a measure of some important factors affecting the microscope performance, such as the presence of mechanical vibrations, electrical interference or thermal drift of the specimen. A measure of the fineness of the detail observable in this type of image may therefore be taken as a measure of 'instrumental resolution'.

2.5.2.10. *Electron diffraction in electron microscopes*

Currently most electron-diffraction patterns are obtained in conjunction with images, in electron microscopes of one form or another, as follows.

(*a*) Selected-area electron-diffraction (SAED) patterns are obtained by using intermediate and projector lenses to form an image of the diffraction pattern in the back-focal plane of the objective lens (Fig. 2.5.2.2). The area of the specimen from which the diffraction pattern is obtained is defined by inserting an aperture in the image plane of the objective lens. For parallel illumination of the specimen, sharp diffraction spots are produced by perfect crystals.

A limitation to the area of the specimen from which the diffraction pattern can be obtained is imposed by the spherical aberration of the objective lens. For a diffracted beam scattered through an angle α, the spread of positions in the object for which the diffracted beam passes through a small axial aperture in the image plane is $C_s\alpha^3$, *e.g.* for $C_s = 1$ mm, $\alpha = 5 \times 10^{-2}$ rad (10,0,0 reflection from gold for 100 keV electrons), $C_s\alpha^3 = 1250$ Å, so that a selected-area diameter of less than about 2000 Å is not feasible. For higher voltages, the minimum selected-area diameter decreases with λ^2 if the usual assumption is made that C_s increases for higher-voltage microscopes so that $C_s\lambda$ is a constant.

(*b*) Convergent-beam electron-diffraction (CBED) patterns are obtained when an incident convergent beam is focused on the specimen, as in an STEM instrument or an STEM attachment for a conventional TEM instrument.

For a large, effectively incoherent source, such as a conventional hot-filament electron gun, the intensities are added for each incident-beam direction. The resulting CBED pattern has an intensity distribution

$$I(uv) = \int |\Psi_{u_1v_1}(uv)|^2 \, \mathrm{d}u_1 \, \mathrm{d}v_1, \qquad (2.5.2.55)$$

where $\Psi_{u_1v_1}(uv)$ is the Fourier transform of the exit wave at the specimen for an incident-beam direction u_1, v_1.

(*c*) Coherent illumination from a small bright source such as a field emission gun may be focused on the specimen to give an electron probe having an intensity distribution $|t(xy)|^2$ and a diameter equal to the STEM dark-field image resolution [equation (2.5.2.47)] of a few Å. The intensity distribution of the resulting microdiffraction pattern is then

$$|\Psi(uv)|^2 = |\Psi_0(uv) * T(uv)|^2, \qquad (2.5.2.56)$$

where $\Psi_0(uv)$ is the Fourier transform of the exit wave at the specimen. Interference occurs between waves scattered from the various incident-beam directions. The diffraction pattern is thus an in-line hologram as envisaged by Gabor (1949).

(*d*) Diffraction patterns may be obtained by using an optical diffractometer (or computer) to produce the Fourier transform squared of a small selected region of a recorded image. The optical diffraction-pattern intensity obtained under the ideal conditions specified under equation (2.5.2.54) is given, in the case of weak phase objects, by

$$I(uv) = \delta(uv) + 4\sigma^2|\Phi(uv)|^2 \cdot \sin^2\chi(uv) \cdot E^2(uv) \qquad (2.5.2.57)$$

or, more generally, by

$$I(uv) = c\delta(uv) + |\Psi(uv) \cdot T(uv) * \Psi^*(uv) \cdot T^*(uv)|^2,$$

where $\Psi(uv)$ is the Fourier transform of the wavefunction at the exit face of the specimen and c is a constant depending on the characteristics of the photographic recording medium.

2.5.3. Space-group determination by convergent-beam electron diffraction* (P. GOODMAN)

2.5.3.1. *Introduction*

2.5.3.1.1. *CBED*

Convergent-beam electron diffraction, originating in the experiments of Kossel and Möllenstedt (Kossel & Möllenstedt, 1938) has been established over the past two decades as a powerful technique for the determination of space group in inorganic materials, with particular application when only microscopic samples are available. Relatively recently, with the introduction of the analytical electron microscope, this technique – abbreviated as CBED – has become available as a routine, so that there is now a considerable accumulation of data from a wide range of materials. A significant extension of the technique in recent times has been the introduction of LACBED (large-angle CBED) by Tanaka & Terauchi (1985). This technique allows an extensive angular range of single diffraction orders to be recorded and, although this method cannot be used for microdiffraction (since it requires an extensive single-crystal area), new LACBED applications appear regularly, particularly in the field of semiconductor research (see Section 2.5.3.6).

The CBED method relies essentially on two basic properties of transmission electron diffraction, namely the radical departure from Friedel's law and the formation of characteristic extinction bands

* Questions related to this section may be addressed to Professor M. Tanaka, Research Institute for Scientific Measurements, Tohoku University, Sendai 980-8577, Japan.

within space-group-forbidden reflections. Departure from Friedel's law in electron diffraction was first noted experimentally by Miyake & Uyeda (1950). The prediction of space-group-forbidden bands (within space-group-forbidden reflections) by Cowley & Moodie (1959), on the other hand, was one of the first successes of *N*-beam theory. A detailed explanation was later given by Gjønnes & Moodie (1965). These are known variously as 'GM' bands (Tanaka *et al.*, 1983), or more simply and definitively as 'GS' (glide–screw) bands (this section). These extinctions have a close parallel with space-group extinctions in X-ray diffraction, with the reservation that only screw axes of order two are accurately extinctive under *N*-beam conditions. This arises from the property that only those operations which lead to identical *projections* of the asymmetric unit can have *N*-beam dynamical symmetries (Cowley *et al.*, 1961).

Additionally, CBED from perfect crystals produces high-order defect lines in the zero-order pattern, analogous to the defect Kikuchi lines of inelastic scattering, which provide a sensitive measurement of unit-cell parameters (Jones *et al.*, 1977; Fraser *et al.*, 1985; Tanaka & Terauchi, 1985).

The significant differences between X-ray and electron diffraction, which may be exploited in analysis, arise as a consequence of a much stronger interaction in the case of electrons (Section 2.5.2). Hence, thin, approximately parallel-sided crystal regions must be used in high-energy (100 kV–1 MV) electron transmission work, so that diffraction is produced from crystals effectively infinitely periodic in only two dimensions, leading to the relaxation of three-dimensional diffraction conditions known as 'excitation error' (Chapter 5.2). Also, there is the ability in CBED to obtain data from microscopic crystal regions of around 50 Å in diameter, with corresponding exposure times of several seconds, allowing a survey of a material to be carried out in a relatively short time.

In contrast, single-crystal X-ray diffraction provides much more limited symmetry information in a direct fashion [although statistical analysis of intensities (Wilson, 1949) will considerably supplement this information], but correspondingly gives much more direct three-dimensional geometric data, including the determination of unit-cell parameters and three-dimensional extinctions.

The relative strengths and weaknesses of the two techniques make it useful where possible to collect both convergent-beam and X-ray single-crystal data in a combined study. However, all parameters *can* be obtained from convergent-beam and electron-diffraction data, even if in a somewhat less direct form, making possible space-group determination from microscopic crystals and microscopic regions of polygranular material. Several reviews of the subject are available (Tanaka, 1994; Steeds & Vincent, 1983; Steeds, 1979). In addition, an atlas of characteristic CBED patterns for direct phase identification of metal alloys has been published (Mansfield, 1984), and it is likely that this type of procedure, allowing *N*-beam analysis by comparison with standard simulations, will be expanded in the near future.

2.5.3.1.2. *Zone-axis patterns from CBED*

Symmetry analysis is necessarily tied to examination of patterns near relevant zone axes, since the most intense *N*-beam interaction occurs amongst the zero-layer zone-axis reflections, with in addition a limited degree of upper-layer (higher-order Laue zone) interaction. There will generally be several useful zone axes accessible for a given parallel-sided single crystal, with the regions between axes being of little use for symmetry analysis. Only one such zone axis can be parallel to a crystal surface normal, and a microcrystal is usually chosen at least initially to have this as the principal symmetry axis. Other zone axes from that crystal may suffer mild symmetry degradation because the *N*-beam lattice component ('excitation error' extension) will not have the symmetry of the structure (Goodman, 1974; Eades *et al.*, 1983).

Upper-layer interactions, responsible for imparting three-dimensional information to the zero layer, are of two types: the first arising from 'overlap' of dynamic shape transforms and causing smoothly varying modulations of the zero-layer reflections, and the second, caused by direct interactions with the upper-layer, or higher-order Laue zone lines, leading to a sharply defined fine-line structure. These latter interactions are especially useful in increasing the accuracy of space-group determination (Tanaka *et al.*, 1983), and may be enhanced by the use of low-temperature specimen stages. The presence of these defect lines in convergent-beam discs, occurring especially in low-symmetry zone-axis patterns, allows symmetry elements to be related to the three-dimensional structure (Section 2.5.3.5; Fig. 2.5.3.4*c*).

To the extent that such three-dimensional effects can be ignored or are absent in the zero-layer pattern the *projection approximation* (Chapter 5.2) can be applied. This situation most commonly occurs in zone-axis patterns taken from relatively thin crystals and provides a useful starting point for many analyses, by identifying the projected symmetry.

2.5.3.2. *Background theory and analytical approach*

2.5.3.2.1. *Direct and reciprocity symmetries: types I and II*

Convergent-beam diffraction symmetries are those of Schrödinger's equation, *i.e.* of crystal potential, plus the diffracting electron. The appropriate equation is given in Section 2.5.2 [equation (2.5.2.6)] and Chapter 5.2 [equation (5.2.2.1)] in terms of the real-space wavefunction ψ. The symmetry elements of the crystal responsible for generating pattern symmetries may be conveniently classified as of two types (I and II) as follows.

I. The *direct* (type I: Table 2.5.3.1) symmetries imposed by this equation on the transmitted wavefunction given z-axis illumination ($\mathbf{k}_0$, the incident wavevector parallel to Z, the surface normal) are just the symmetries of φ whose operation leaves both crystal and z axis unchanged. These are also called 'vertical' symmetry elements, since they contain Z. These symmetries apply equally in real and reciprocal space, since the operator ∇^2 has circular symmetry in both spaces and does nothing to degrade the symmetry in

Table 2.5.3.1. *Listing of the symmetry elements relating to CBED patterns under the classifications of 'vertical' (I), 'horizontal' (II) and combined or roto-inversionary axes*

I. Vertical symmetry elements		
	International symbols	
	$2, 3, 4, 6$ $(2_1, 3_1, \ldots)$	
	m (c)	
	a, b (n)	
II. Horizontal symmetry elements		
	Diperiodic symbols	BESR symbols
	$2'$	m
	$2'_1$	
	m'	1_R
	a', b', n'	
	$\bar{1}'$	2_R
I + II	$\bar{4}'$	4_R
I × II	$\bar{3}' = 3 \times \bar{1}'$	$6_R = 3 \cdot 2_R$
	$\bar{6}' = 3 \times m'$	31_R

transmission. Hence, for high-symmetry crystals (zone axis parallel to z axis), and to a greater or lesser degree for crystals of a more general morphology, these zone-axis symmetries apply both to electron-microscope lattice images and to convergent-beam patterns under z-axis-symmetrical illumination, and so impact also on space-group determination by means of high-resolution electron microscopy (HREM). In CBED, these elements lead to *whole pattern* symmetries, to which every point in the pattern contributes, regardless of diffraction order and Laue zone (encompassing ZOLZ and HOLZ reflections).

II. Reciprocity-induced symmetries, on the other hand, depend upon ray paths and path reversal, and in the present context have relevance only to the diffraction pattern. Crystal-inverting or horizontal crystal symmetry elements combine with reciprocity to yield *indirect* pattern symmetries lacking a one-to-one real-space correspondence, within individual diffraction discs or between disc pairs. Type II elements are assumed to lie on the central plane of the crystal, midway between surfaces, as symmetry operators; this assumption amounts to a 'central plane' approximation, which has a very general validity in space-group-determination work (Goodman, 1984*a*).

A minimal summary of basic theoretical points, otherwise found in Chapter 5.2 and numerous referenced articles, is given here.

For a specific zero-layer diffraction order $g\ (= h, k)$ the incident and diffracted vectors are $\mathbf{k}_0$ and $\mathbf{k}_g$. Then the three-dimensional vector $\mathbf{K}_{0g} = \frac{1}{2}(\mathbf{k}_0 + \mathbf{k}_g)$ has the pattern-space projection, $\mathbf{K}_g = {}^{p}[\mathbf{K}_{0g}]$. The point $\mathbf{K}_g = \mathbf{0}$ gives the *symmetrical Bragg condition* for the associated diffraction disc, and $\mathbf{K}_g \neq \mathbf{0}$ is identifiable with the angular deviation of $\mathbf{K}_{0g}$ from the vertical z axis in three-dimensional space (see Fig. 2.5.3.1). $\mathbf{K}_g = \mathbf{0}$ also defines the symmetry centre within the two-dimensional disc diagram (Fig. 2.5.3.2); namely, the intersection of the lines S and G, given by the trace of excitation error, $\mathbf{K}_g = \mathbf{0}$, and the perpendicular line directed towards the reciprocal-space origin, respectively. To be definitive it is necessary to index diffracted amplitudes relating to a fixed crystal thickness and wavelength, with both crystallographic and momentum coordinates, as $\mathbf{u}_{g,K}$, to handle the continuous variation of $\mathbf{u}_g$ (for a particular diffraction order), with angles of incidence as determined by $\mathbf{k}_0$, and registered in the diffraction plane as the projection of $\mathbf{K}_{0g}$.

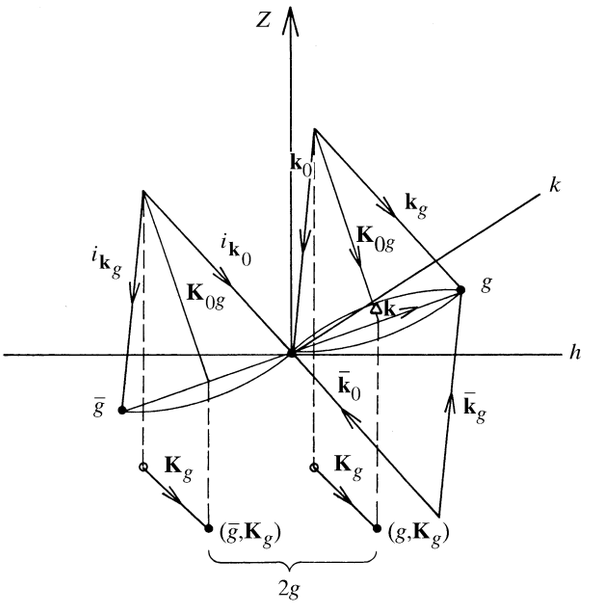

Fig. 2.5.3.1. Vector diagram in semi-reciprocal space, using Ewald-sphere constructions to show the 'incident', 'reciprocity' and 'reciprocity × centrosymmetry' sets of vectors. Dashed lines connect the full vectors $\mathbf{K}_{0g}$ to their projections $\mathbf{K}_g$ in the plane of observation.

2.5.3.2.2. *Reciprocity and Friedel's law*

Reciprocity was introduced into the subject of electron diffraction in stages, the essential theoretical basis, through Schrödinger's equation, being given by Bilhorn *et al.* (1964), and the N-beam diffraction applications being derived successively by von Laue (1935), Cowley (1969), Pogany & Turner (1968), Moodie (1972), Buxton *et al.* (1976), and Gunning & Goodman (1992).

Reciprocity represents a reverse-incidence configuration reached with the reversed wavevectors $\bar{\mathbf{k}}_0 = -\mathbf{k}_g$ and $\bar{\mathbf{k}}_g = -\mathbf{k}_0$, so that the scattering vector $\Delta\mathbf{k} = \mathbf{k}_g - \mathbf{k}_0 = \bar{\mathbf{k}}_0 - \bar{\mathbf{k}}_g$ is unchanged, but $\bar{\mathbf{K}}_{0g} = \frac{1}{2}(\bar{\mathbf{k}}_0 + \bar{\mathbf{k}}_g)$ is changed in sign and hence reversed (Moodie, 1972). The reciprocity equation,

$$\mathbf{u}_{g,\mathbf{K}} = \mathbf{u}^{*}_{g,\bar{\mathbf{K}}}, \tag{2.5.3.1}$$

is valid independently of crystal symmetry, but cannot contribute symmetry to the pattern unless a crystal-inverting symmetry element is present (since $\bar{\mathbf{K}}$ belongs to a reversed wavevector). The simplest case is centrosymmetry, which permits the right-hand side of (2.5.3.1) to be complex-conjugated giving the useful CBED pattern equation

$$\mathbf{u}_{g,\mathbf{K}} = \mathbf{u}_{\bar{g},\mathbf{K}}. \tag{2.5.3.2}$$

Since $\mathbf{K}$ is common to both sides there is a point-by-point identity between the related distributions, separated by $2g$ (the distance between g and $\bar{g}$ reflections). This invites an obvious analogy with *Friedel's law*, $F_g = F^{*}_{\bar{g}}$, with the reservation that (2.5.3.2) holds only for centrosymmetric crystals. This condition (2.5.3.2) constitutes what has become known as the $\pm H$ symmetry and, incidentally, is the only reciprocity-induced symmetry so general as to not depend upon a disc symmetry-point or line, nor on a particular zone axis (*i.e.* it is not a point symmetry but a translational symmetry of the pattern intensity).

2.5.3.2.3. *In-disc symmetries*

(*a*) *Dark-field (diffracted-beam) discs*. Other reciprocity-generated symmetries which are available for experimental observation relate to a single (zero-layer) disc and its origin $\mathbf{K}_g = \mathbf{0}$, and are summarized here by reference to Fig. 2.5.3.2, and given in operational detail in Table 2.5.3.2. The notation subscript R, for reciprocity-induced symmetries, introduced by Buxton *et al.* (1976) is now adopted (and referred to as BESR notation). Fig.

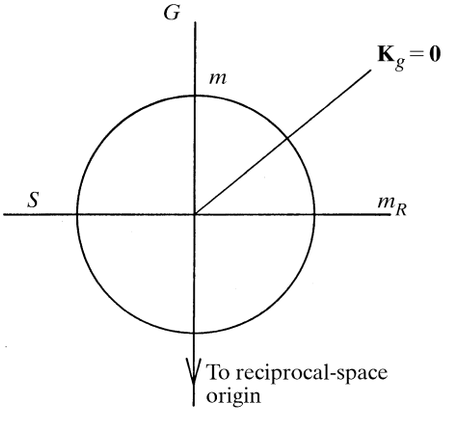

Fig. 2.5.3.2. Diagrammatic representation of a CBED disc with symmetry lines m, m_R (alternate labels G, S) and the central point $\mathbf{K}_g = 0$.

2.5.3.2 shows a disc crossed by reference lines m and m_R. These will be mirror lines of intensity if: (*a*) **g** is parallel to a vertical mirror plane; and (*b*) **g** is parallel to a horizontal diad axis, respectively. The third possible point symmetry, that of disc centrosymmetry (1_R in BESR notation) will arise from the presence of a horizontal mirror plane. Lines m and m_R become the GS extinction lines G and S when glide planes and screw axes are present instead of mirror planes and diad axes.

(*b*) *Bright-field (central-beam) disc*. The central beam is a special case since the point $\mathbf{K}_0 = \mathbf{0}$ is the centre of the whole pattern as well as of that particular disc. Therefore, both sets of rotational symmetry (types I and II) discussed above apply (see Table 2.5.3.3).

In addition, the central-beam disc is a source of three-dimensional lattice information from defect-line scattering. Given a sufficiently perfect crystal this fine-line structure overlays the more general intensity modulation, giving this disc a lower and more precisely recorded symmetry.

2.5.3.2.4. *Zero-layer absences*

Horizontal glides, a', n' (diperiodic, primed notation), generate zero-layer absent rows, or centring, rather than GS bands (see Fig. 2.5.3.3). This is an example of the projection approximation in its most universally held form, *i.e.* in application to absences. Other examples of this are: (*a*) appearance of both G and S extinction bands near their intersection irrespective of whether glide or screw axes are involved; and (*b*) suppression of the influence of vertical, non-primitive translations with respect to observations in the zero layer. It is generally assumed as a working rule that the zero-layer or ZOLZ pattern will have the rotational symmetry of the point-group component of the vertical screw axis (so that $2_1 \simeq 2$). Elements included in Table 2.5.3.1 on this pretext are given in parentheses. However, the presence of 2_1 rather than 2 (3_1 rather than 3 *etc.*) should be detectable as a departure from accurate twofold symmetry in the first-order-Laue-zone (FOLZ) reflection circle (depicted in Fig. 2.5.3.3). This has been observed in the cubic structure of $Ba_2Fe_2O_5Cl_2$, permitting the space groups $I23$ and $I2_13$ to be distinguished (Schwartzman *et al.*, 1996). A summary of all the symmetry components described in this section is given diagrammatically in Table 2.5.3.2.

2.5.3.3. *Pattern observation of individual symmetry elements*

The following guidelines, the result of accumulated experience from several laboratories, are given in an experimentally based sequence, and approximately in order of value and reliability.

(i) The value of X in an *X-fold rotation* axis is made immediately obvious in a zone-axis pattern, although a screw component is not detected in the pattern symmetry.

Roto-inversionary axes require special attention: $\bar{6}$ and $\bar{3}$ may be factorized, as in Tables 2.5.3.1, 2.5.3.3 and 2.5.3.4, to show better the additional CBED symmetries ($3/m'$ and $3 \times \bar{1}'$, respectively). $\bar{4}$ cannot be decomposed further (Table 2.5.3.1) and generates its own diffraction characteristics in non-projective patterns (see Section 2.5.3.5). This specific problem of observing the fourfold roto-

Table 2.5.3.2. *Diagrammatic illustrations of the actions of five types of symmetry elements (given in the last column in Volume A diagrammatic symbols) on an asymmetric pattern component, in relation to the centre of the pattern at* $\mathbf{K}_{00} = \mathbf{0}$*, shown as '* $\oplus$*', or in relation to the centre of a diffraction order at* $\mathbf{K}_{0g} = \mathbf{0}$*, shown as '+'*

Type	Symmetry element	Observation and action	In combination	Interpretation
Vertical	4			
	m; a	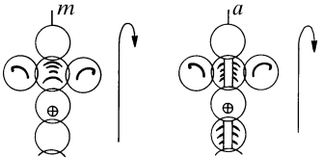	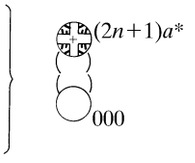	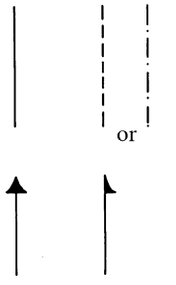
Horizontal	$2'$; $2'_1$	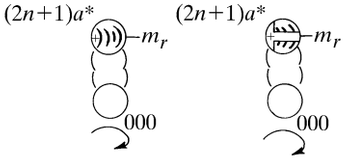		
	$i(\bar{1}')$	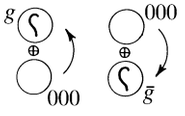		
	m'; a'	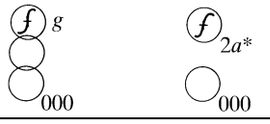		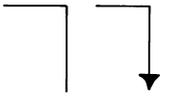

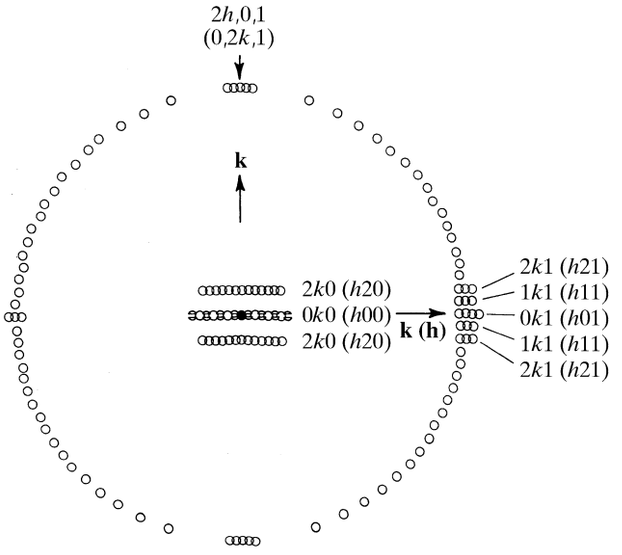

Fig. 2.5.3.3. Diagrammatic representation of the influence of non-symmorphic elements: (i) Alternate rows of the zero-layer pattern are absent owing to the horizontal glide plane. The pattern is indexed as for an '*a*' glide; the alternative indices (in parentheses) apply for a '*b*' glide. (ii) GS bands are shown along the central row of the zero layer, for odd-order reflections.

inversion symmetry has been resolved recently by Tanaka *et al.* (1994) using both CBED and LACBED techniques.

(ii) *Vertical mirror plane* determination may be the most accurate crystal point-symmetry test, given that it is possible to follow the symmetry through large crystal rotations (say 5 to 15°) about the mirror normal. It is also relatively unaffected by crystal surface steps as compared to (v) below.

(iii) *Horizontal glide planes* are determined unequivocally from zero-layer absences when the first Laue zone is recorded, either with the main pattern or by further crystal rotation; *i.e.* a section of this zone is needed to determine the lateral unit-cell parameters. This observation is illustrated diagrammatically in Fig. 2.5.3.3.

(iv) An extinction (GS) line or band through odd-order reflections of a zone-axis pattern indicates only a *projected glide line*. This is true because both $P2_1$ (No. 4) and *Pa* (No. 7) symmetries project into '*pg*' in two dimensions. However, the projection approximation has only limited validity in CBED. For all crystal rotations *around* the 2_1 axis, or alternatively *about the glide-plane 'a' normal*, dynamic extinction conditions are retained. This is summarized by saying that the diffraction vector $\mathbf{K}_{0g}$ should be either normal to a screw axis or contained within a glide plane for the generation of the *S* or *G* bands, respectively. Hence $P2_1$ and *Pa* may be distinguished by these types of rotations away from the zone axis with the consequence that the element 2_1 in particular is characterized by extinctions close to the Laue circle for the tilted ZOLZ pattern (Goodman, 1984*b*), and that the glide *a* will generate extinction bands through both ZOLZ and HOLZ reflections for all orientations maintaining Laue-circle symmetry about the *S* band (Steeds *et al.*, 1978).

As a supplement to this, in a refined technique not universally applicable, Tanaka *et al.* (1983) have shown that fine-line detail from HOLZ interaction can be observed which will separately identify *S*- (2_1) and *G*-band symmetry from a single pattern (see Fig. 2.5.3.6).

(v) The centre-of-symmetry (or $\pm H$) test can be made very sensitive by suitable choice of diffraction conditions but requires a reasonably flat crystal since it involves a pair of patterns (the angular beam shift involved is very likely to be associated with some lateral probe shift on the specimen). This test is best carried out at a low-symmetry zone axis, free from other symmetries, and preferably incorporating some fine-line HOLZ detail, in the following way. The hkl and $\bar{h}\bar{k}\bar{l}$ reflections are successively illuminated by accurately exchanging the central-beam aperture with the diffracted-beam apertures, having first brought the zone axis on to the electron-microscope optic axis. This produces the symmetrical $\pm H$ condition.

(vi) In seeking internal m_R symmetry as a test for a horizontal diad axis it is as well to involve some distinctive detail in the mirror symmetry (*i.e.* simple two-beam-like fringes should be avoided), and also to rotate the crystal about the supposed diad axis, to avoid an m_R symmetry due to projection [for examples see Fraser *et al.* (1985) and Goodman & Whitfield (1980)].

(vii) The presence or absence of the in-disc centrosymmetry element 1_R formally indicates the presence or absence of a horizontal mirror element m', either as a true mirror or as the mirror component of a horizontal glide plane g'. In this case the *absence* of symmetry provides more positive evidence than its presence, since absence is sufficient evidence for a lack of central-mirror crystal symmetry but an observed symmetry could arise from the operation of the projection approximation. If some evidence of the three-dimensional interaction is included in the observation or if three-dimensional interaction (from a large *c* axis parallel to the zone axis) is evident in the rest of the pattern, this latter possibility can be excluded. Interpretation is also made more positive by extending the angular aperture, especially by the use of LACBED.

These results are illustrated in Table 2.5.3.2 and by actual examples in Section 2.5.3.5.

2.5.3.4. *Auxiliary tables*

Space groups may very well be identified using CBED patterns from an understanding of the diffraction properties of real-space symmetry elements, displayed for example in Table 2.5.3.2. It is, however, of great assistance to have the symmetries tabulated in reciprocal space, to allow direct comparison with the pattern symmetries.

There are three generally useful ways in which this can be done, and these are set out in Tables 2.5.3.3 to 2.5.3.5. The simplest of these is by means of point group, following the procedures of Buxton *et al.* (1976). Next, the CBED pattern symmetries can be listed as diperiodic groups which are space groups in two dimensions, allowing identification with a restricted set of three-dimensional space groups (Goodman, 1984*b*). Finally, the dynamic extinctions (GS bands and zero-layer absences) can be listed for each non-symmorphic space group, together with the diffraction conditions for their observation (Tanaka *et al.*, 1983; Tanaka & Terauchi, 1985). Descriptions for these tables are given below.

Table 2.5.3.3. BESR symbols (Buxton *et al.*, 1976) incorporate the subscript *R* to describe reciprocity-related symmetry elements, *R* being the operator that rotates the disc pattern by 180° about its centre. The symbols formed in this way are $1_R, 2_R, 4_R, 6_R$, where X_R represents $2\pi/X$ rotation about the zone axis, followed by *R*. Of these, 2_R represents the $\pm H$ symmetry (two twofold rotations) described earlier [equation (2.5.3.2)] as a transformation of crystalline centrosymmetry; 6_R may be thought of as decomposing into $3 \cdot 2_R$ for purposes of measurement. The mirror line m_R (Fig. 2.5.3.2) is similarly generated by $m \cdot 1_R$.

Table 2.5.3.3 gives the BESR interrelation of pattern symmetries with point group (Buxton *et al.*, 1976; Steeds, 1983). Columns I and II of the table list the point symmetries of the whole pattern and bright-field pattern, respectively; column III gives the BESR diffraction groups. [*Note:* following the Pond & Vlachavas (1983) usage, '*' has been appended to the centrosymmetric groups.]

Table 2.5.3.3. *Diffraction point-group tables, giving whole-pattern and central-beam pattern symmetries in terms of BESR diffraction-group symbols and diperiodic group symbols*

I	II	III	IV	V	
				Cubic point groups	
Whole pattern	Bright field (central beam)	BESR group	Diperiodic group (point group)	[100]	[110]
1	1	1	1		
1	2	$\underline{1}_R$	m'		
2	2	2	2		
1	1	$^*2_R$	$\bar{1}'$		
2	2	$^*\underline{21}_R$	$2/m'$		
1	m	m_R	$2'$		23
m	m	m	m		
m	$2mm$	$\underline{m1}_R$	$2'mm'$		$\bar{4}3m$
2	$2mm$	$2m_Rm_R$	$2'2'2$	23	432
$2mm$	$2mm$	$2mm$	$mm2$		
m	m	$^*2_Rmm_R$	$2'/m$		$m\bar{3}$
$2mm$	$2mm$	$^*\underline{2mm1}_R$	mmm'	$m\bar{3}$	$m\bar{3}m$
4	4	4	4		
2	4	4_R	$\bar{4}'$		
4	4	$^*\underline{41}_R$	$4/m'$		
4	$4mm$	$4m_Rm_R$	$42'2'$	$\bar{4}32$	
$4mm$	$4mm$	$4mm$	$4mm$		
$2mm$	$4mm$	4_Rmm_R	$\bar{4}'m2'$	$\bar{4}3m$	
$4mm$	$4mm$	$^*\underline{4mm1}_R$	$4/m'mm$	$m\bar{3}m$	
3	3	3	3		
3	6	$\underline{31}_R$	$\bar{6}'$		
3	$3m$	$3m_R$	$32'$		
$3m$	$3m$	$3m$	$3m$		
$3m$	$6mm$	$\underline{3m1}_R$	$\bar{6}'m2'$		
6	6	6	6		
3	3	$^*6_R$	$\bar{3}'$		
6	6	$^*\underline{61}_R$	$6/m'$		
6	$6mm$	$6m_Rm_R$	$62'2'$		
$6mm$	$6mm$	$6mm$	$6mm$		
$3m$	$3m$	$^*6_Rmm_R$	$\bar{3}'m$		
$6mm$	$6mm$	$^*\underline{6mm1}_R$	$6/m'mm$		

Inspection of columns I and II shows that 11 of the 31 diffraction groups can be determined from a knowledge of the whole pattern and bright-field (central-beam disc) point symmetries alone. The remaining 10 pairs of groups need additional observation of the dark-field pattern for their resolution. Disc symmetries 1_R, m_R (Fig. 2.5.3.2; Table 2.5.3.2) are sought (*a*) in general zero-layer discs and (*b*) in discs having an m_R line perpendicular to a proposed twofold axis, respectively; the $\pm H$ test is applied for centrosymmetry, to complete the classification.

Column IV gives the equivalent diperiodic point-group symbol, which, unprimed, gives the corresponding three-dimensional symbol. This will always refer to a non-cubic point group. Column V gives the additional cubic point-group information indicating, where appropriate, how to translate the diffraction symmetry into [100] or [110] cubic settings, respectively.

Of the groups listed in column III, those representing the projection group of their class are underlined. These groups all contain 1_R, the BESR symbol for m'. When the projection approximation is applicable, only those groups underlined will apply. The effect of this approximation is to add a horizontal mirror plane to the symmetry group.

Table 2.5.3.4. This lists possible space groups for each of the classified zero-layer CBED symmetries. Since the latter constitute the 80 diperiodic groups, it is first necessary to index the pattern in diperiodic nomenclature; the set of possible space groups is then given by the table.

A basic requirement for diperiodic group nomenclature has been that of compatibility with *IT* A and I. This has been met by the recent Pond & Vlachavas (1983) tabulation. For example, DG: $(^*)pban'$, where * indicates centrosymmetry, becomes space group *Pban* when, in Seitz matrix description, the former group matrix is multiplied by the third primitive translation, a_3. Furthermore, in textual reference the prime can be optionally omitted, since the lower-case lattice symbol is sufficient indication of a two-dimensional periodicity (as *pban*).

The three sections of Table 2.5.3.4 are:

I. Point-group entries, given in H–M and BESR symbols.

II. Pattern symmetries, in diperiodic nomenclature, have three subdivisions: (i) symmorphic groups: patterns without zero-layer absences or extinctions. Non-symmorphic groups are then given in two categories: (ii) patterns with zero-layer GS bands, and (iii) patterns with zero-layer absences resulting from a horizontal glide plane; where the pattern *also* contains dynamic extinctions (GS bands) and so is listed in column (ii), the column (iii) listing is given in parentheses.

The 'short' (Pond & Vlachavas) symbol has proved an adequate description for all but nine groups for which the screw-axis content was needed: here $(2'_1)$, or $(2'_12'_1)$, have been added to the symbol.

III. Space-group entries are given in terms of *IT* A numbers. The first column of each row gives the same-name space group as illustrated by the example $pban' \rightarrow Pban$ above. The groups following in the same row (which have the same zero-layer symmetry) complete an exhaustive listing of the II*b* subgroups, given in *IT* A. Cubic space groups are underlined for the sake of clarity; hence, those giving rise to the zero-layer symmetry of the diffraction group in the [100] (cyclic) setting have a single underline: these are type I minimal supergroups in *IT* A nomenclature. The cubic groups are also given in the [110] setting, in underlined italics, since this is a commonly encountered high-symmetry setting. (*Note*: these then are no longer *minimal* supergroups and the relationship has to be found through a series of *IT* A listings.)

The table relates to maximal-symmetry settings. For monoclinic and orthorhombic systems there are three equally valid settings. For monoclinic groups, the oblique and rectangular settings appear separately; where rectangular *C*-centred groups appear in a second setting this is indicated by superscript '2'. For orthorhombic groups, superscripts correspond to the 'incident-beam' system adopted in Table 2.5.3.5, as follows: no superscript: [001] beam direction; superscript 1: [100] beam direction; superscript 2: [010] beam direction. The cubic system is treated specially as described above.

Table 2.5.3.5. This lists conditions for observation of GS bands for the 137 space groups exhibiting these extinctions. These are entered as '*G*', '*S*', or '*GS*', indicating whether a glide plane, screw axis, or both is responsible for the GS band. All three possibilities will lead to a glide line (and hence to both extinction bands) in projection, and one of the procedures (*a*), (*b*), or (*c*) of Section 2.5.3.3(iv) above is needed to complete the three-dimensional interpretation. In addition, the presence of horizontal glide planes, which result in systematic absences in these particular cases in the zero-layer pattern, is indicated by the symbol '–'. Where these occur at the site of prospective '*G*' or '*S*' bands from other glide or

screw elements the symbol of that element is given and the '*G*' or '*S*' symbol is omitted.

The following paragraphs give information on the real-space interpretation of GS band formation, and their specific extinction rules, considered useful in structural interpretation.

Real-space interpretation of extinction conditions. Dynamic extinctions (GS bands) are essentially a property of symmetry in reciprocal space. However, since diagrams from *IT* I and A are used there is a need to give an equivalent real-space description. These bands are associated with the half-unit-cell-translational glide planes and screw axes represented in these diagrams. Inconsistencies between 'conventional' and 'physical' real-space descriptions, however, become more apparent in dynamical electron diffraction, which is dependent upon three-dimensional scattering physics, than in X-ray diffraction. Also, the distinction between general (symmorphic) and specific (non-symmorphic) extinctions is more basic (in the former case). This is clarified by the following points:

(i) Bravais lattice centring restricts the conditions for observation of GS bands. For example, in space group *Abm*2 (No. 39), '*A*' centring prevents observation of the GS bands associated with the '*b*' glide at the [001] zone-axis orientation; this observation, and hence verification of the *b* glide, must be made at the lower-symmetry zone axes [0*vw*] (see Table 2.5.3.5). In the exceptional cases of space groups $I2_12_12_1$ and $I2_13$ (Nos. 24 and 199), conditions for the observation of the relevant GS bands are completely prevented by body centring; here the screw axes of the symmorphic groups *I*222 and *I*23 are parallel to the screw axes of their non-symmorphic derivatives. However, electron crystallographic methods also include direct structure imaging by HREM, and it is important to note here that while the indistinguishability encountered in data sets acquired in Fourier space applies to both X-ray diffraction and CBED (notwithstanding possible differences in HOLZ symmetries), this limitation does not apply to the HREM images (produced by dynamic scattering) yielding an approximate structure image for the (zone-axis) *projection*. This technique then becomes a powerful tool in space-group research by supplying phase information in a different form.

(ii) A different complication, relating to nomenclature, occurs in the space groups $P\bar{4}3n$, *Pn*3*n* and *Pm*3*n* (Nos. 218, 222 and 223) where '*c*' glides parallel to a diagonal plane of the unit cell occur as primary non-symmorphic elements (responsible for reciprocal-space extinctions) but are not used in the Hermann–Maugin symbol; instead the derivative '*n*' glide planes are used as characters, resulting in an *apparent* lack of correspondence between the conventionally given real-space symbols and the reciprocal-space extinctions.

(*Note*: In *IT* I non-symmorphic reflection rules which duplicate rules given by lattice centring, or those which are a consequence of more general rules, are given in parentheses; in *IT* A this clarification by parenthesizing, helpful for electron-diffraction analysis, has been removed.)

(iii) Finally, diamond glides (symbol '*d*') require special consideration since they are associated with translations $\frac{1}{4}, \frac{1}{4}, \frac{1}{4}$, and so would appear not to qualify for GS bands; however, this translation is a result of the conventional cell being defined in real rather than reciprocal space where the extinction symmetry is formed. Hence '*d*' glides occur only in *F*-centred lattices (most obviously Nos. 43, 70, 203, 277 and 228). These have correspondingly an *I*-centred reciprocal lattice for which the zero-layer two-dimensional unit cell has an edge of $a^{*\prime\prime} = 2a^*$. Consequently, the first-order row reflection along the diamond glide retains the reciprocal-space anti-symmetry on the basis of this physical unit cell (halved in real space), and leads to the labelling of odd-order reflections as $4n + 2$ (instead of $2n + 1$ when the cell is not halved). Additionally, although seven space groups are *I*-centred in real space with the conventional unit cell (Nos. 109, 110, 122, 141, 142, 220 and 230), these space groups are *F*-centred with the transformation $a'' = [110]$, $b'' = [1\bar{1}0]$, and correspondingly *I*-centred in the reciprocal-space cell as before, but the directions [100], [010] and reflection rows *h*00, 0*k*0 become replaced by directions [110] (or [1$\bar{1}$0]) and rows *hh*0, *h*$\bar{h}$0, in the entries of Table 2.5.3.5.

Extinction rules for symmetry elements appearing in Table 2.5.3.5. Reflection indices permitting observation of *G* and *S* bands follow [here 'zero-layer' and 'out-of-zone' (*i.e.* HOLZ or alternative zone) serve to emphasize that these are zone-axis observations].

(i) *Vertical glide planes* lead to '*G*' bands in reflections as listed ('*a*', '*b*', '*c*' and '*n*' glides):

*h*0*l*, *hk*0, 0*kl* out-of-zone reflections (for glide planes having normals [010], [001] and [100]) having $h + l$, $h + k$, $k + l = 2n + 1$, respectively, in the case of '*n*' glides, or *h*, *k*, *l* odd in the case of '*a*', '*b*' or '*c*' glides, respectively;

*h*00, 0*k*0, 00*l* zero-layer reflections with *h*, *k* or *l* odd.

Correspondingly for '*d*' glides:

(*a*) In *F*-centred cells:

*h*0*l*, *hk*0, 0*kl* out-of-zone reflections (for glide planes having normals [010], [100] and [001], having $h + l$, $k + l$, or $h + k = 4n + 2$, respectively, with *h*, *k* and *l* even; and (space group No. 43 only) zero-layer reflections *h*00, 0*k*0 with *h*, *k* even and $= 4n + 2$.

(*b*) In *I*-centred cells:

hhl (cyclic on *h*, *k*, *l* for cubic groups) out-of-zone reflections having $2h + l = 4n + 2$, with *l* even; and zero-layer reflections *hh*0, *h*$\bar{h}$0 (cyclic on *h*, *k*, *l* for cubic groups) having *h* odd.

(ii) *Horizontal screw axes*, namely 2_1 or the 2_1 component of screw axes 4_1, 4_3, 6_1, 6_3, 6_5, lead to '*S*' bands in reflection rows parallel to the screw axis, *i.e.* either *h*00, 0*k*0 or 00*l*, with conventional indexing, for *h*, *k* or *l* odd.

(iii) *Horizontal glide planes* lead to zero-layer absences rather than GS bands. When these prevent observation of a specific GS band (by removing the two-dimensional conditions), the symbol '−' indicates a situation where, in general, there will simply be absences for the odd-order reflections. However, Ishizuka & Taftø (1982) were the first to observe finite-intensity narrow bands under these conditions, and it is now appreciated that with a sufficient crystal thickness and a certain minimum for the *z*-axis repeat distance, GS bands can be recorded by violating the condition for horizontal-mirror-plane (m') extinction while satisfying the condition for *G* or *S*, achieved by appropriate tilts away from the exact zone-axis orientation [see Section 2.5.3.3(iv)].

2.5.3.5. *Space-group analyses of single crystals; experimental procedure and published examples*

2.5.3.5.1. *Stages of procedure*

(i) *Zone-axis patterns*. The first need is to record a principal zone-axis pattern. From this, the rotational order *X* of the vertical axis and associated mirror (including glide-line) components are readily observed (see all examples).

This pattern may include part of the higher-order Laue zone; in particular the closest or first-order Laue zone (FOLZ) should be included in order to establish the presence or absence of horizontal glide planes, as illustrated in Fig. 2.5.3.3. The projection approximation frequently applies to the zone-axis pattern, particularly when this is obtained from thin crystals (although this cannot apply by definition to the FOLZ). This is indicated by the absence of fine-line detail in the central beam particularly; identification of the projected symmetry is then straightforward.

(ii) *Laue circle patterns*. Next, it is usual to seek patterns in which discs around the Laue circle include the line m_R (Fig.

2.5.3.2). The internal disc symmetries observed together with those from the zone-axis pattern will determine a diffraction group, classifying the zero-layer symmetry. [Fig. 6(*c*) of Goodman & Whitfield (1980) gives an example of Laue-circle symmetries.]

(iii) *Alternative zone axes or higher-order Laue zones*. Finally, alternative zone or higher-order Laue-zone patterns may be sought for additional three-dimensional data: (*a*) to determine the three-dimensional extinction rules, (*b*) to test for centrosymmetry, or (*c*) to test for the existence of mirror planes perpendicular to the principal rotation axis. These procedures are illustrated in the following examples.

2.5.3.5.2. *Examples*

(1) *Determination of centrosymmetry; examples from the hexagonal system*. Fig. 2.5.3.4(*a*) illustrates the allocation of planar point groups from [0001] zone-axis patterns of β-Si_3N_4 (left-hand side) and β-GaS (right-hand side); the patterns exhibit point symmetries of 6 and 6*mm*, respectively, as indicated by the accompanying geometric figures, permitting point groups 6 or $6/m$, and 6*mm* or $6/mmm$, in three dimensions. Alternative zone axes are required to distinguish these possibilities, the actual test used (testing for the element m' or the centre of symmetry) being largely determined in practice by the type of crystal preparation.

Fig. 2.5.3.4(*b*) shows the CBED pattern from the $[11\bar{2}0]$ zone axis of β-Si_3N_4 (Bando, 1981), using a crystal with the corresponding cleavage faces. The breakdown of Friedel's law between reflections 0002 and $000\bar{2}$ rules out the point group $6/m$ (the element m' from the first setting is not present) and establishes 6 as the correct point group.

Also, the GS bands in the 0001 and $000\bar{1}$ reflections are consistent with the space group $P6_3$. [*Note*: screw axes 6_1, 6_3 and 6_5 are not distinguished from these data alone (Tanaka *et al.*, 1983).]

Fig. 2.5.3.4(*c*) shows CBED patterns from the vicinity of the $[1\bar{1}02]$ zone axis of β-GaS, only 11.2° rotated from the [0001] axis and accessible using the same crystal as for the previous [0001] pattern. This shows a positive test for centrosymmetry using a conjugate reflection pair $1\bar{1}01/\bar{1}10\bar{1}$, and establishes the centrosymmetric point group $\bar{6}/mmm$, with possible space groups Nos. 191, 192, 193 and 194. Rotation of the crystal to test the extinction rule for $hh2\bar{h}l$ reflections with l odd (Goodman & Whitfield, 1980) establishes No. 194 ($P6_3/mmc$) as the space group.

Comment: These examples show two different methods for testing for centrosymmetry. The $\pm H$ test places certain requirements on the specimen, namely that it be reasonably accurately parallel-sided – a condition usually met by easy-cleavage materials like GaS, though not necessarily by the wedge-shaped refractory Si_3N_4 crystals. On the other hand, the 90° setting, required for direct observation of a possible perpendicular mirror plane, is readily available in these fractured samples, but not for the natural cleavage samples.

(2) *Point-group determination in the cubic system, using Table 2.5.3.3*. Fig. 2.5.3.5 shows [001] (cyclic) zone-axis patterns from two cubic materials, which serve to illustrate the ability to distinguish cubic point groups from single zone-axis patterns displaying detailed central-beam structures. The left-hand pattern, from the mineral gahnite (Ishizuka & Taftø, 1982) has 4*mm* symmetry in *both* the whole pattern and the central (bright-field) beam, permitting only the BESR group $4mm1_R$ for the cubic system (column III, Table 2.5.3.3); this same observation establishes the crystallographic point group as $m3m$ (column V of Table 2.5.3.3). The corresponding pattern for the χ-phase precipitate of stainless steel (Steeds & Evans, 1980) has a whole-pattern symmetry of only 2*mm*, lower than the central-beam (bright-field) symmetry of 4*mm* (this lower symmetry is made clearest from the innermost reflections bordering the central beam). This combination leads to the BESR group 4_Rmm_R (column III, Table 2.5.3.3), and identifies the cubic point group as $\bar{4}3m$.

(3) *Analysis of data from FeS_2 illustrating use of Tables 2.5.3.4 and 2.5.3.5*. FeS_2 has a cubic structure for which a complete set of data has been obtained by Tanaka *et al*. (1983); the quality of the data makes it a textbook example (Tanaka & Terauchi, 1985) for demonstrating the interpretation of extinction bands.

Figs. 2.5.3.6(*a*) and (*b*) show the [001] (cyclic) exact zone-axis pattern and the pattern with symmetrical excitation of the 100 reflection, respectively (Tanaka *et al.*, 1983).

(i) Using Table 2.5.3.4, since there are GS bands, the pattern group must be listed in column II(ii); since a horizontal '*b*' glide plane is present (odd rows are absent in the b^* direction), the symbol must contain a 'b'' (or 'a'') (*cf.* Fig. 2.5.3.3). The only possible cubic group from Table 2.5.3.4 is No. 205.

(ii) Again, a complete GS cross, with both *G* and *S* arms, is present in the 100 reflection (central in Fig. 2.5.3.6*b*), confirmed by mirror symmetries across the *G* and *S* lines. From Table 2.5.3.5 only space group No. 205 has the corresponding entry in the column for '[100] cyclic' with *GS* in the cubic system (space groups Nos. 198–230). Additional patterns for the [110] setting, appearing in the original paper (Tanaka *et al.*, 1983), confirm the cubic system, and also give additional extinction characteristics for 001 and $1\bar{1}0$ reflections (Tanaka *et al.*, 1983; Tanaka & Terauchi, 1985).

(4) *Determination of centrosymmetry and space group from extinction characteristics*. Especially in working with thin crystals used in conjunction with high-resolution lattice imaging, it is sometimes most practical to determine the point group (*i.e.* space-group class) from the dynamic extinction data. This is exemplified in the Moodie & Whitfield (1984) studies of orthorhombic materials. Observations on the zero-layer pattern for Ge_3SbSe_3 with a point symmetry of 2*mm*, and with GS extinction bands along odd-order *h*00 reflections, together with missing reflection rows in the 0*k*0 direction, permit identification from Table 2.5.3.4. This zone-axis pattern has the characteristics illustrated in Figs. 2.5.3.3 and hence (having both missing rows and GS bands) should be listed in both II(ii) and II(iii). Hence the diffraction group must be either No. 40 or 41. Here, the class *mmm*, and hence centrosymmetry, has been identified through non-symmorphic elements.

This identification leaves seven possible space groups, Nos. 52, 54, 56, 57, 60, 61 and 62, to be distinguished by *hkl* extinctions.

The same groups are identified from Table 2.5.3.5 by seeking the entry *GS* '−' in one of the [001] (cyclic) entries for the orthorhombic systems. With the assumption that no other principal zone axis is readily available from the same sample (which will generally be true), Table 2.5.3.5, in the last three columns, indicates which *minor* zone axes should be sought in order to identify the space group, from the glide-plane extinctions of '*G*' bands. For example, space group 62 has no *h*0*l* extinctions, but will give 0*kl* extinction bands '*G*' according to the rules for an '*n*' glide, *i.e.* in reflections for which $k + l = 2n + 1$. Again, if the alternative principal settings *are* available (from the alternative cleavages of the sample) the correct space group can be found from the first three columns of Table 2.5.3.5.

From the above discussions it will be clear that Tables 2.5.3.4 and 2.5.3.5 present information in a complementary way: in Table 2.5.3.4 the specific pattern group is indexed first with the possible space groups following, while in Table 2.5.3.5 the space group is indexed first, and the possible pattern symmetries are then given, in terms of the standard *International Tables* setting.

2.5.3.6. *Use of CBED in study of crystal defects, twins and non-classical crystallography*

(i) Certain crystal defects lend themselves to analysis by CBED and LACBED. In earlier work, use was made of the high sensitivity

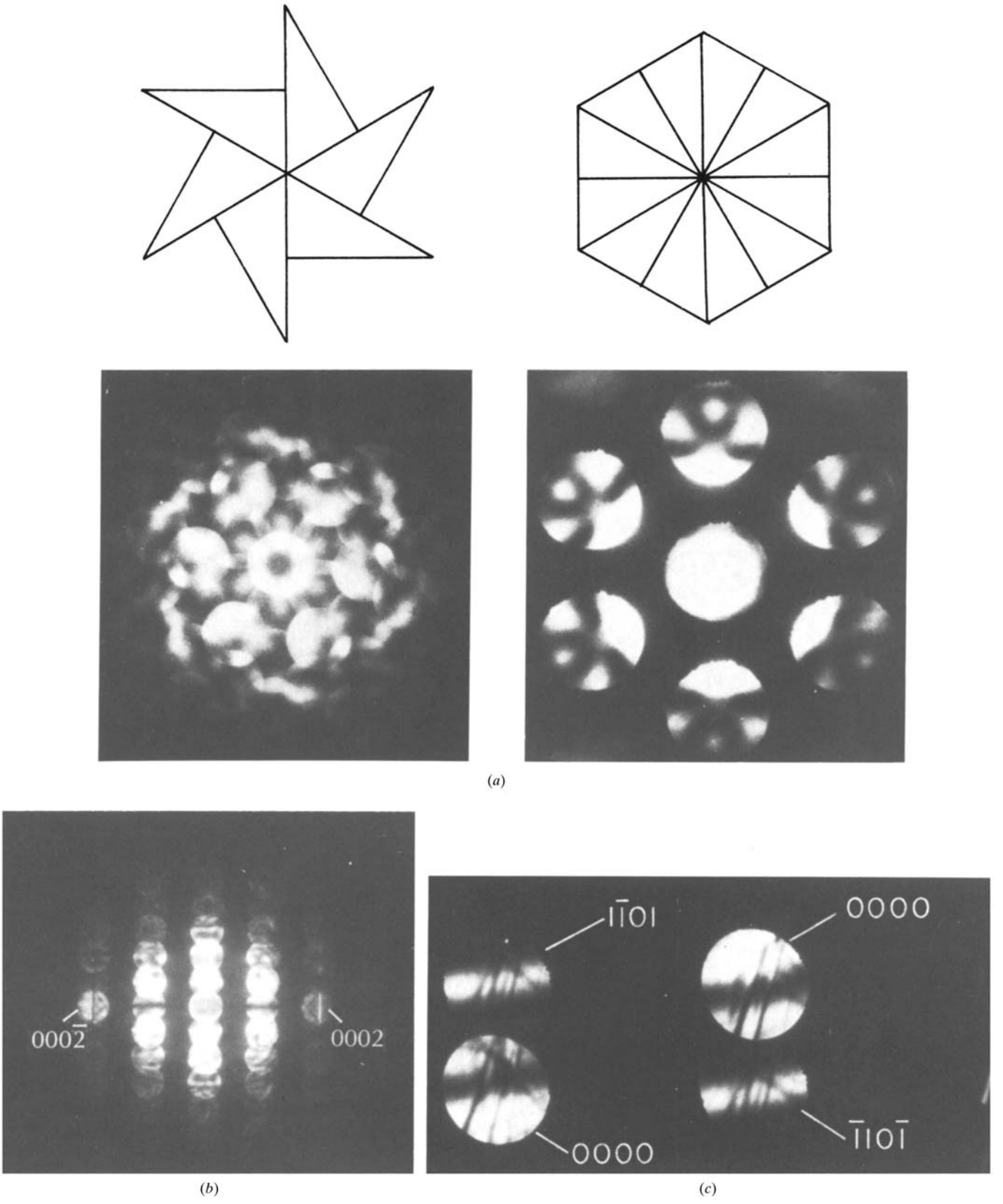

Fig. 2.5.3.4. (*a*) Zone-axis patterns from hexagonal structures β-Si_3N_4 (left) and β-GaS (right) together with the appropriate planar figures for point symmetries 6 and 6*mm*, respectively. (*b*) $[12\bar{1}0]$ zone-axis pattern from β-Si_3N_4, showing Friedel's law breakdown in symmetry between 0002 and $000\bar{2}$ reflections (Bando, 1981). (*c*) Conjugate pair of $1\bar{1}01/\bar{1}101$ patterns from β-GaS, taken near the $[1102]$ zone axis, showing a translational symmetry associated with structural centrosymmetry.

of HOLZ line geometry to unit-cell parameters (Jones *et al.*, 1977). A computer program (Tanaka & Terauchi, 1985) is available for simulating relative line positions from lattice geometry, assuming kinematical scattering, which at least provides a valid starting point since these spacings are mainly determined from geometric considerations. Fraser *et al.* (1985), for example, obtained a sensitivity of 0.03% in measurements of cubic-to-tetragonal distortions in this way, although the absolute accuracy was not established.

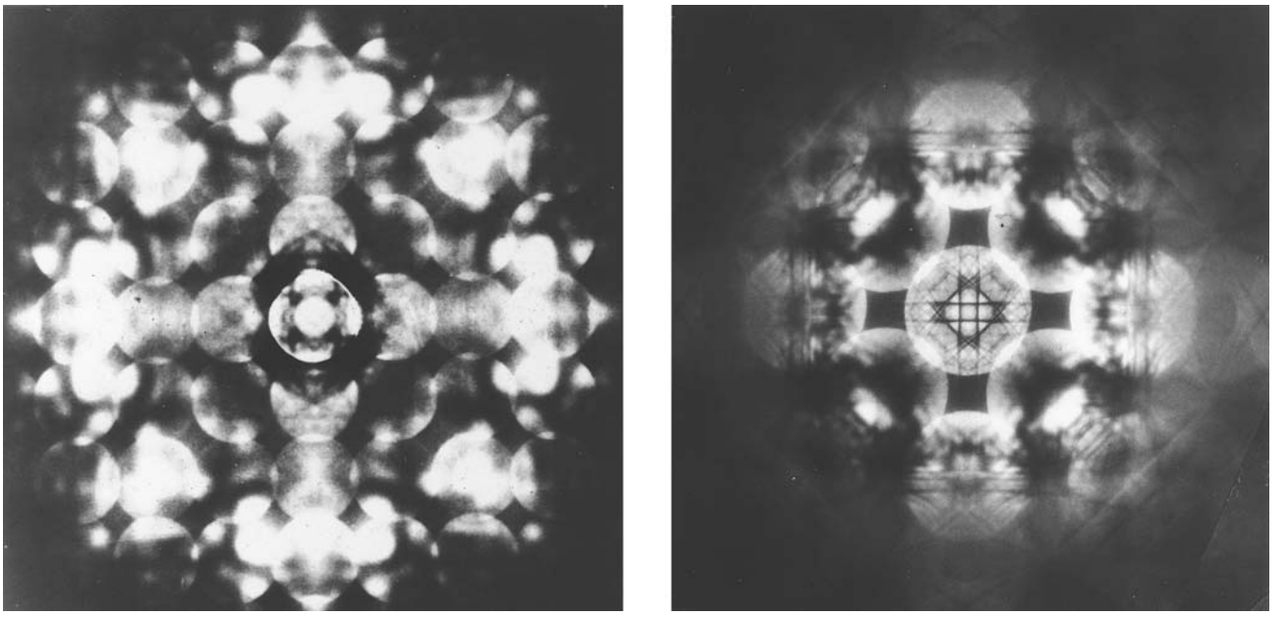

Fig. 2.5.3.5. Zone-axis patterns from cubic structures gahnite (left) (Ishizuka & Taftø, 1982) and χ-phase precipitate (right) (Steeds & Evans, 1980).

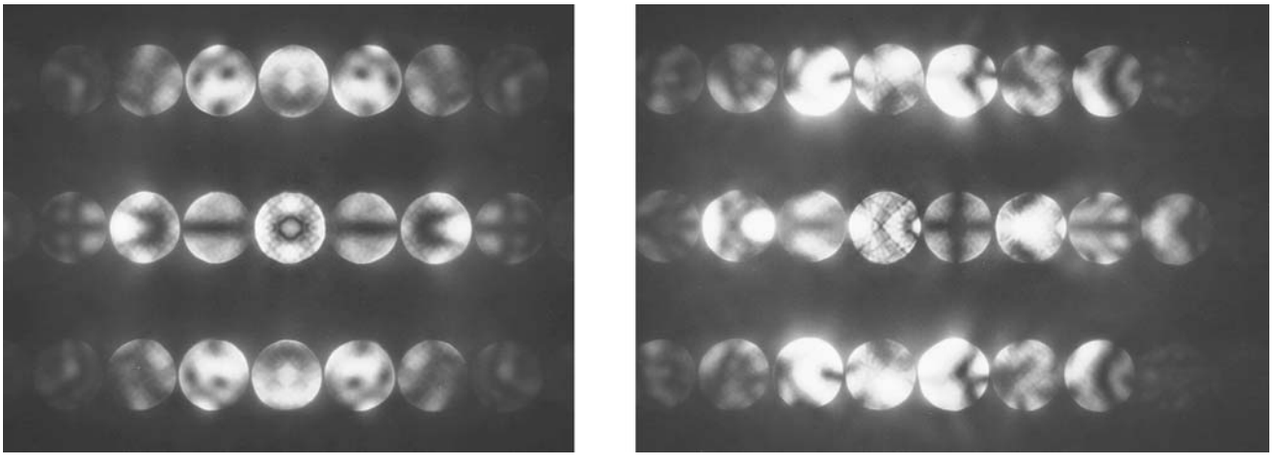

Fig. 2.5.3.6. (*a*) CBED pattern from the exact [001] (cyclic) zone-axis orientation of FeS_2. (*b*) Pattern from the [001] zone axis oriented for symmetrical excitation of the 100 reflection (central in the printed pattern) [from the collection of patterns presented in Tanaka *et al.* (1983); originals kindly supplied by M. Tanaka].

(ii) By contrast, techniques have been devised for evaluating Bragg-line splitting caused by the action of a strain field within the single crystal. One method depends upon the observation of splitting in HOLZ lines (Carpenter & Spence, 1982). More recently, the use of LACBED has allowed quantitative evaluation of lattice distortions in semiconductor heterostructures (*e.g.* containing GaAs–InGaAs interfaces). This technique has been reviewed by Chou *et al.* (1994).

(iii) Quite distinct from this is the analysis of stacking faults between undistorted crystal domains (Johnson, 1972). Coherent twin boundaries with at least a two-dimensional coincidence site lattice can be considered in a similar fashion (Schapink *et al.*, 1983). In marked contrast to electron-microscopy image analysis these boundaries need to be parallel (or nearly so) to the crystal surfaces rather than inclined or perpendicular to them for analysis by CBED or LACBED.

The term 'rigid-body displacement' (RBD) is used when it is assumed that no strain field develops at the boundary. A classification of the corresponding bi-crystal symmetries was developed by Schapink *et al.* (1983) for these cases. Since experimental characterization of grain boundaries is of interest in metallurgy, this represents a new area for the application of LACBED and algorithms invoking reciprocity now make routine *N*-beam analysis feasible.

The original investigations, of a mid-plane stacking fault in graphite (Johnson, 1972) and of a mid-plane twin boundary in gold (Schapink *et al.*, 1983), represent classic examples of the influence of bi-crystal symmetry on CBED zone-axis patterns, whereby the changed central-plane symmetry is transformed through reciprocity into an exact diffraction symmetry. (*a*) In the graphite ($P6_3/mmc$) example, the hexagonal pattern of the unfaulted graphite is replaced by a trigonal pattern with mid-plane faulting. Here a mirror plane at

the centre of the perfect crystal (*A–B–A* stacking) is replaced by an inversion centre at the midpoint of the single rhombohedral cell *A–B–C*; the projected symmetry is also reduced from hexagonal to trigonal: both whole pattern and central beam then have the symmetry of $3m1$. The $2H$ polytype of TaS_2 ($P6_3/mmc$) (Tanaka & Terauchi, 1985) gives a second clear example. (*b*) In the case of a [111] gold crystal, sectioning the f.c.c. structure parallel to [111] preparatory to producing the twin already reduces the finite crystal symmetry to $R\bar{3}m$, *i.e.* a trigonal space group for which the central beam, and the HOLZ reflections in particular, exhibit the trigonal symmetry of $31m$ (rather than the $3m1$ of trigonal graphite). A central-plane twin boundary with no associated translation introduces a central horizontal mirror plane into the crystal. For the zone-axis pattern the only symmetry change will be in the central beam, which will become centrosymmetric, increasing its symmetry to $6mm$. Using diffraction-group terminology these cases are seen to be relative inverses. Unfaulted graphite has the BESR group $6mm1_R$ (central beam and whole pattern hexagonal); central-plane faulting results in a change to the group 6_Rmm_R. Unfaulted [111] gold correspondingly has the BESR group symmetry 6_Rmm_R; central-plane twinning results in the addition of the element 1_R (for a central mirror plane), leading to the group $6mm1_R$.

(iv) Finally, no present-day discussion of electron-crystallographic investigations of symmetry could be complete without reference to two aspects of non-classical symmetries widely discussed in the literature in recent years. The recent discovery of noncrystallographic point symmetries in certain alloys (Shechtman *et al.*, 1984) has led to the study of quasi-crystallinity. An excellent record of the experimental side of this subject may be found in the book *Convergent-beam electron diffraction III* by Tanaka *et al.* (1994), while the appropriate space-group theory has been developed by Mermin (1992). It would be inappropriate to comment further on this new subject here other than to state that this is clearly an area of study where combined HREM, CBED and selected-area diffraction (SAD) evidence is vital to structural elucidation.

The other relatively new topic is that of modulated structures. From experimental evidence, two distinct structural phenomena can be distinguished for structures exhibiting incommensurate superlattice reflections. Firstly, there are 'Vernier' phases, which exist within certain composition ranges of solid solutions and are composed of two extensive substructures, for which the superspace-group nomenclature developed by de Wolff *et al.* (1981) is structurally valid (*e.g.* Withers *et al.*, 1993). Secondly, there are structures essentially composed of random mixtures of two or more substructures existing as microdomains within the whole crystal (*e.g.* Grzinic, 1985). Here the SAD patterns will contain superlattice reflections with characteristic profiles and/or irregularities of spacings. A well illustrated review of incommensurate-structure analysis in general is given in the book by Tanaka *et al.* (1994), while specific discussions of this topic are given by Goodman *et al.* (1992), and Goodman & Miller (1993).

2.5.3.7. *Present limitations and general conclusions*

The list of examples given here must necessarily be regarded as unsatisfactory considering the vastness of the subject, although some attempt has been made to choose a diverse range of problems which will illustrate the principles involved. Some particular aspects, however, need further mention.

One of these concerns the problem of examining large-unit-cell materials with a high diffraction-pattern density. This limits the possible convergence angle, if overlap is to be avoided, and leaves numerous but featureless discs [for example Goodman (1984*b*)]. Technical advances which have been made to overcome this problem include the beam-rocking technique (Eades, 1980) and LACBED (Tanaka *et al.*, 1980), both of which are reviewed by Tanaka & Terauchi (1985) and Eades *et al.* (1983). The disadvantage of these latter methods is that they both require a significantly larger area of specimen than does the conventional technique, and it may be that more sophisticated methods of handling the crowded conventional patterns are still needed.

Next, the matter of accuracy must be considered. There are two aspects of the subject where this is of concern. Firstly, there is a very definite limit to the sensitivity with which symmetry can be detected. In a simple structure of medium-light atoms, displacements of say 0.1 Å or less from a pseudomirror plane could easily be overlooked. An important aspect of CBED analysis, not mentioned above, is the *N*-beam computation of patterns which is required when something approaching a refinement (in the context of electron diffraction) is being attempted. Although this quantitative aspect has a long history [for example see Johnson (1972)], it has only recently been incorporated into symmetry studies as a routine (Creek & Spargo, 1985; Tanaka, 1994). Multi-slice programs which have been developed to produce computer-simulated pattern output are available (Section 2.5.3.8).

Next there is concern as to the allocation of a space group to structures which microscopically have a much lower symmetry (Goodman *et al.*, 1984). This arises because the volume sampled by the electron probe necessarily contains a large number of unit cells. Reliable microscopic interpretation of certain nonstoichiometric materials requires that investigations be accompanied by high-resolution microscopy. Frequently (especially in mineralogical samples), nonstoichiometry implies that a space group exists only on average, and that the concept of absolute symmetry elements is inapplicable.

From earlier and concluding remarks it will be clear that combined X-ray/CBED and CBED/electron-microscopy studies of inorganic materials represents the standard ideal approach to space-group analysis at present; given this approach, all the space-group problems of classical crystallography appear soluble. As has been noted earlier, it is important that HREM be considered jointly with CBED in determining space group by electron crystallography, and that only by this joint study can the so-called 'phase problem' be completely overcome. The example of the space-group pairs $I222/I2_12_12_1$ and $I23/I2_13$ has already been cited. Using CBED, it might be expected that FOLZ lines would show a break from twofold symmetry with the incident beam aligned with a 2_1 axis. However, a direct distinction should be made apparent from high-resolution electron micrographs. Other less clear-cut cases occur where the HREM images allow a space-group distinction to be made between possible space groups of the same arithmetic class, especially when only one morphology is readily obtained (*e.g.* $P222_1$, $P22_12_1$, $P2_12_12_1$).

The slightly more subtle problem of distinguishing enantiomorphic space-group pairs can be solved by one of two approaches: either the crystal must be rotated around an axis by a known amount to obtain two projections, or the required three-dimensional phase information can be deduced from specific three-beam-interaction data. This problem is part of the more general problem of solving handedness in an asymmetric structure, and is discussed in detail by Johnson & Preston (1994).

2.5.3.8. *Computer programs available*

(1) A FORTRAN source listing of program *TCBED* for simulating three-dimensional convergent-beam patterns with absorption by the Bloch-wave method: Zuo *et al.* (1989) [see also *Electron microdiffraction* (Spence & Zuo, 1992) for other useful programs and worked examples for the analysis of these diffraction

(*continued on page* 306)

Table 2.5.3.4. *Tabulation of principal-axis CBED pattern symmetries against relevant space groups given as IT A numbers*

Three columns of diperiodic groups (central section) correspond to (i) symmorphic groups, (ii) non-symmorphic groups (GS bands) and (iii) non-symmorphic groups (zero-layer absences arising from horizontal glide planes). Cubic space groups are given underlined in the right-hand section with the code: underlining = [001](cyclic) setting; italics + underlining = [110](cyclic) setting. Separators ';' and ':' indicate change of Bravais lattice type and change of crystal system, respectively.

	I Point groups		II Diperiodic groups				III Space groups
DG	H–M	BESR	(i)	(ii)	(iii)	SG	Subgroups II*b* (Subgroups 1)
Oblique						Triclinic	
1	1	1	$p1$			1	
2*	$\bar{1}$	2_R	$p\bar{1}'$			2	
						Monoclinic (Oblique)	
3	12	2	$p2$			3	4, 5
4	$1m$	1_R	pm'			6	8
5	$1m$				pb'	7	9
6*	$2/m$	21_R	$p2/m'$			10	11, 12
7*	$2/m$	21_R			$p2/b'$	13	14, 15
Rectangular						(Rectangular)	
8	21	m_R	$p2'$			3	5^2: *195*; *197*, *199*
9	21	m_R		$p2_1'$		4	*198*
10	21	m_R	$c2'$			5	*196*
11	$m1$	m	pm			6^2	7, 8^2
12	$m1$	m		pa		7^2	9^2
13	$m1$	m	cm			8	9
14*	$12/m$	2_Rmm_R	$p2'/m$			10	13, 12^2: *200*, *201*; *204*
15*	$12/m$	2_Rmm_R		$p2_1'/m$		11	14
16*	$12/m$	2_Rmm_R		$p2'/a$		13^2	15^2: *206*
17*	$12/m$	2_Rmm_R		$p2_1'/m$		14^2	*205*
18*	$12/m$	2_Rmm_R	$c2'/m$			12	15: *202*, *203*
						Orthorhombic	
19	222	$2m_Rm_R$	$p2'2'2$			16	17; 21^2; 22: 195; 196, *207*, *206*; *211*, *214*
20	222	$2m_Rm_R$		$p2_1'2'2$		17^2	18^2; 20^2: *212*, *213*
21	222	$2m_Rm_R$		$p2_1'2_1'2$		18	19: 198
22	222	$2m_Rm_R$	$c2'2'2$			21	20; 23, 24: 197, 199, *209*, *210*
23	$mm2$	$2mm$	$pmm2$			25	26, 27; 38, 39; 42
24	$mm2$	$2mm$		$pbm2$		28	29, 30, 31^2; 40, 41
25	$mm2$	$2mm$		$pba2$		32	33, 34; 43
26	$mm2$	$2mm$	$cmm2$			35	36, 37; 44, 45, 46
27	$mm2$	$m1_R$	$p2'mm'$			25^2	28^1; 35^2, 42^2; 38^2, 39^2: *215*; *217*
28	$mm2$	$m1_R$		$p2_1'm'a$		26^1	31^1; 36^1
29	$mm2$	$m1_R$		$p2_1'ab'$	$(p2_1'ab')$	29^2	33^2
30	$mm2$	$m1_R$			$p2_1'ma'$	26^2	29^1; 36^2
31	$mm2$	$m1_R$			$p2_1'mn'$	31^2	33^2
32	$mm2$	$m1_R$			$p2'mb'$	28^2	32^2, 40^2, 41^2
33	$mm2$	$m1_R$			$p2'aa'$	27^2	30^2; 37^2
34	$mm2$	$m1_R$			$pb2'n'$	30^1	34^2; 43^2: *218*; *219*
35	$mm2$	$m1_R$	$c2'mm'$			38^1	40^1; 44^2, 46^1: *216*; *220*
36	$mm2$	$m1_R$			$c2'mb'$	39^1	41^1; 45^2, 46^2
37*	mmm	$2mm1_R$	$pmmm'$			47	49, 51^1; 65^2, 67^2; 69: *200*; *202*, *221*, *224*, *226*, *228*, *229*
38*	mmm	$2mm1_R$		$pbmm'$ $(2_1')$		51^2	53^1, 57, 59^2; 63^1, 64^1
39*	mmm	$2mm1_R$		$pbam'$ $(2_1'2_1')$		55	58, 62^2
40*	mmm	$2mm1_R$		$pmab'$ $(2_1'2_1')$	$(pmab')$	57^1	60^2, 61, 62: 205
41*	mmm	$2mm1_R$		$pbaa'$ $(2_1')$	$(pbaa')$	54^2	52, 56^2, 60^1

Table 2.5.3.4. *Tabulation of principal-axis CBED pattern symmetries against relevant space groups given as IT A numbers* (*cont.*)

	I Point groups		II Diperiodic groups				III Space groups
DG	H–M	BESR	(i)	(ii)	(iii)	SG	Subgroups II*b* (Subgroups 1)
42*	*mmm*	$2mm1_R$			$pmma'$ $(2'_1)$	51	54, 55^2, 57^2; 63^2, 64^2
43*	*mmm*	$2mm1_R$			$pmmn'$ $(2'_12'_1)$	59	56, 62^1
44*	*mmm*	$2mm1_R$			$pbmn'$ $(2'_1)$	53^2	52^1, 58^1, 60
45*	*mmm*	$2mm1_R$			$pmaa'$	49^2	50^2, 53, 54^1; 66^2, 68^1: 222, 223
46*	*mmm*	$2mm1_R$			$pban'$	50	52^2, 48; 70: 201; 203, 230
47*	*mmm*	$2mm1_R$	$cmmm'$			65	63, 66; 72, 74^2, 71: 204, 225, 227
48*	*mmm*	$2mm1_R$			$cmma'$	67	64, 68; 72^1, 74, 73: 206
Square						Tetragonal	
49	4	4	$p4$			75	77, 76, 78; 79, 80
50	$4/m$	41_R	$p4/m'$			83	84; 87
51	$4/m$	41_R			$p4/n'$	85	86, 88
52	422	$4m_Rm_R$	$p42'2'$			89	93, 91, 95; 97, 98: 207, 208; 209, 210; 211, 214
53	422	$4m_Rm_R$		$p42'_12'$		90	94, 92, 96: 212, 213
54	$4mm$	$4mm$	$p4mm$			99	101, 103, 105; 107, 108
55	$4mm$	$4mm$		$p4bm$		100	102, 104, 106; 109, 110
56*	$4/mmm$	$4mm1_R$	$p4/m'mm$			123	124, 131, 132; 139, 140; 221, 223; 225, 226; 229
57*	$4/mmm$	$4mm1_R$		$p4/m'bm$ $(2'_1)$		127	128, 135, 136
58*	$4/mmm$	$4mm1_R$			$p4/n'bm$	125	126, 133, 134; 141, 142: 222, 224; 227, 228; 230
59*	$4/mmm$	$4mm1_R$			$p4/n'mm$ $(2'_1)$	129	130, 137, 138
60	$\bar{4}$	4_R	$p\bar{4}'$			81	82
61	$\bar{4}2m$	4_Rmm_R	$p\bar{4}'m\bar{2}'$			115	116; 119, 120
62	$\bar{4}2m$	4_Rmm_R		$p\bar{4}b2'$		117	118; 122: 220
63	$\bar{4}2m$	4_Rmm_R	$p\bar{4}'2'm$			111	112; 121: 215; 216; 217; 218; 219
64	$\bar{4}2m$	4_Rmm_R		$p4'2'_1m$		113	114
Hexagonal						Trigonal	
65	3	3	$p3$			143	144, 145; 146
66	$\bar{3}$	6_R	$p\bar{3}'$			147	148
67	32	$3m_R$	$p312'$			149	151, 153
68	32	$3m_R$	$p32'1$			150	152, 154; 155
69	$3m$	$3m$	$p31m$			157	159
70	$3m$	$3m$	$p3m1$			156	158; 160, 161
71*	$\bar{3}m$	6_Rmm_R	$p\bar{3}'1m$			162	163
72*	$\bar{3}m$	6_Rmm_R	$p\bar{3}'m1$			164	165; 166, 167
						Hexagonal	
73	6	6	$p6$			168	171, 172, 173, 169, 170
74	$\bar{6}$	31_R	$p3/m'$ $(p\bar{6}')$			174	
75	622	$6m_Rm_R$	$p62'2'$			177	180, 181, 182, 178, 179
76	$6mm$	$6mm$	$p6mm$			183	184, 185, 186
77*	$6/m$	61_R	$p6/m'$			175	176
78*	$6/mmm$	$6mm1_R$	$p6/m'mm$			191	192, 193, 194
79	$\bar{6}m2$	$3m1_R$	$p3/m'2'm$ $(p\bar{6}'m2')$			189	190
80	$\bar{6}m2$	$3m1_R$	$p3/m'm2'$ $(p\bar{6}'2'm)$			187	188

Table 2.5.3.5. *Conditions for observation of GS bands for the 137 space groups exhibiting these extinctions*

Point groups 2, *m*, 2/*m* (2nd setting unique axis $\|b$)

Space group		Incident-beam direction [$u0w$]
4	$P2_1$	$0k0$ 2_1 S
7	Pc	$h0l$ c G
9	Cc	$h0l$ c G
11	$P2_1/m$	$0k0$ 2_1 S
13	$P2/c$	$h0l$ c G
14	$P2_1/c$	$0k0$ 2_1 S $h0l$ c G
15	$C2/c$	$h0l$ c G

Point groups 222, *mm*2

Space group		Incident-beam direction					
		[100]	[010]	[001]	[$uv0$]	[$0vw$]	[$u0w$]
17	$P222_1$	$00l$ 2_1 S	$00l$ 2_1 S		$00l$ 2_1 S		
18	$P2_12_12$	$0k0$ 2_1 S	$h00$ 2_1 S	$h00$, $0k0$ 2_1 S		$h00$ 2_1 S	$0k0$ 2_1 S
19	$P2_12_12_1$	$0k0$, $00l$ 2_1 S	$h00$, $00l$ 2_1 S	$h00$, $0k0$ 2_1 S	$00l$ 2_1 S	$h00$ 2_1 S	$0k0$ 2_1 S
20	$C222_1$	$00l$ 2_1 S	$00l$ 2_1 S		$00l$ 2_1 S		
26	$Pmc2_1$	$00l$ $c+2_1$ GS	$00l$ 2_1 $c'-$		$00l$ 2_1 S		$h0l$ c G
27	$Pcc2$	$00l$ c $c'-$	$00l$ c $c'-$			$0kl$ c G	$h0l$ c G
28	$Pma2$			$h00$ a G			$h0l$ a G
29	$Pca2_1$	$00l$ 2_1 $c'-$	$00l$ $c+2_1$ GS	$h00$ a G	$00l$ 2_1 S	$0kl$ c G	$h0l$ a G
30	$Pnc2$	$00l$ c $n'-$	$00l$ n $c'-$	$0k0$ n G		$0kl$ n G	$h0l$ c G
31	$Pmn2_1$	$00l$ $n+2_1$ GS	$00l$ 2_1 $n'-$	$h00$ n G	$00l$ 2_1 S		$h0l$ n G
32	$Pba2$			$h00$, $0k0$ a b G		$0kl$ b G	$h0l$ a G

Table 2.5.3.5. *Conditions for observation of GS bands for the 137 space groups exhibiting these extinctions* (*cont.*)

Space group		Incident-beam direction					
		[100]	[010]	[001]	[uv0]	[0vw]	[u0w]
33	$Pna2_1$	00l 2_1 $n'-$	00l $n+2_1$ GS	h00, 0k0 a b G	00l 2_1 S	0kl n G	h0l a G
34	$Pnn2$	00l n $n'-$	00l n $n'-$	h00, 0k0 n G		0kl n G	h0l n G
36	$Cmc2_1$	00l $c+2_1$ GS	00l 2_1 $c'-$		00l 2_1 S		h0l c G
37	$Ccc2$	00l c $c'-$	00l c $c'-$			0kl c G	h0l c G
39	$Abm2$					0kl b G	
40	$Ama2$			h00 a G			h0l a G
41	$Aba2$			h00 a G		0kl b G	h0l a G
43	$Fdd2$	00l $d'-$	00l d $d'-$	h00, 0k0 d G		0kl d G	h0l d G
45	$Iba2$	$b'-$	$a'-$			0kl b G	h0l a G
46	$Ima2$		$a'-$				h0l a G

Point group *mmm*

Space group		Incident-beam direction					
		[100]	[010]	[001]	[uv0]	[0vw]	[u0w]
48	$P\,2/n\,2/n\,2/n$	00l, 0k0 n $n'-$	00l, h00 n $n'-$	0k0, h00 n $n'-$	hk0 n G	0kl n G	h0l n G
49	$P\,2/c\,2/c\,2/m$	00l c $c'-$	00l c $c'-$			0kl c G	h0l c G
50	$P\,2/b\,2/a\,2/n$	0k0 n $b'-$	h00 n $a'-$	0k0, h00 b a $n'-$	hk0 n G	0kl b G	h0l a G
51	$P\,2_1/m\,2/m\,2/a$		h00 $a+2_1$ GS	h00 2_1 $a'-$	hk0 a G	h00 2_1 S	
52	$P\,2/n\,2_1/n\,2/a$	00l, 0k0 n 2_1 $a'-$	00l, h00 n a $n'-$	0k0 $n+2_1$ GS h00 n $n'-$	hk0 a G	0kl n G	h0l n G 0k0 2_1 S
53	$P\,2/m\,2/n\,2_1/a$	00l $n+2_1$ GS	h00, 00l a 2_1 $a'-$	h00 n $a'-$	hk0 a G 00l 2_1 S		h0l n G

Table 2.5.3.5. *Conditions for observation of GS bands for the 137 space groups exhibiting these extinctions* (*cont.*)

Space group		Incident-beam direction					
		[100]	[010]	[001]	[*uv*0]	[0*vw*]	[*u*0*w*]
54	$P\,2_1/c\,2/c\,2/a$	$00l$ c $c'-$	$h00$ $a+2_1$ *GS* $00l$ c $c'-$	$h00$ 2_1 $a'-$	$hk0$ a *G*	$0kl$ c *G* $h00$ 2_1 *S*	$h0l$ c *G*
55	$P\,2_1/b\,2_1/a\,2/m$	$0k0$ 2_1 $b'-$	$h00$ 2_1 $a'-$	$0k0, h00$ $b+2_1, a+2_1$ *GS*		$0kl$ b *G* $h00$ 2_1 *S*	$h0l$ a *G* $0k0$ 2_1 *S*
56	$P\,2_1/c\,2_1/c\,2/n$	$0k0$ $n+2_1$ *GS* $00l$ c $c'-$	$h00$ $n+2_1$ *GS* $00l$ c $c'-$	$0k0, h00$ 2_1 $n'-$	$hk0$ n *G*	$0kl$ c *G* $h00$ 2_1 *S*	$h0l$ c *G* $0k0$ 2_1 *S*
57	$P\,2/b\,2_1/c\,2_1/m$	$00l$ $c+2_1$ *GS* $0k0$ 2_1 $b'-$	$00l$ 2_1 $c'-$	$0k0$ $b+2_1$ *GS*	$00l$ 2_1 *S*	$0kl$ b *G*	$h0l$ c *G* $0k0$ 2_1 *S*
58	$P\,2_1/n\,2_1/n\,2/m$	$00l, 0k0$ $n\quad 2_1$ $n'-$	$00l, h00$ $n\quad 2_1$ $n'-$	$0k0, h00$ $n+2_1$ *GS*		$0kl$ n *G* $h00$ 2_1 *S*	$h0l$ n *G* $0k0$ 2_1 *S*
59	$P\,2_1/m\,2_1/m\,2/n$	$0k0$ $n+2_1$ *GS*	$h00$ $n+2_1$ *GS*	$0k0, h00$ 2_1 $n'-$	$hk0$ n *G*	$h00$ 2_1 *S*	$0k0$ 2_1 *S*
60	$P\,2_1/b\,2/c\,2_1/n$	$00l$ $c+2_1$ *GS* $0k0$ n $b'-$	$h00$ $n+2_1$ *GS* $00l$ 2_1 $c'-$	$0k0, h00$ $b\quad 2_1$ $n'-$	$hk0$ n *G* $00l$ 2_1 *S*	$0kl$ b *G* $h00$ 2_1 *S*	$h0l$ c *G*
61	$P\,2_1/b\,2_1/c\,2_1/a$	$00l$ $c+2_1$ *GS* $0k0$ 2_1 $b'-$	$h00$ $a+2_1$ *GS* $00l$ 2_1 $c'-$	$0k0$ $b+2_1$ *GS* $h00$ 2_1 $a'-$	$hk0$ a *G* $00l$ 2_1 *S*	$0kl$ b *G* $h00$ 2_1 *S*	$h0l$ c *G* $0k0$ 2_1 *S*
62	$P\,2_1/n\,2_1/m\,2_1/a$	$0k0, 00l$ 2_1 $n'-$	$00l$ $n+2_1$ *GS* $h00$ $a+2_1$	$0k0$ $n+2_1$ *GS* $h00$ 2_1 $a'-$	$hk0$ a *G* $00l$ 2_1 *S*	$0kl$ n *G* $h00$ 2_1 *S*	$0k0$ 2_1 *S*
63	$C\,2/m\,2/c\,2_1/m$	$00l$ $c+2_1$ *GS*	$00l$ 2_1 $c'-$		$00l$ 2_1 *S*		$h0l$ c *G*
64	$C\,2/m\,2/c\,2_1/a$	$00l$ $c+2_1$ *GS*	$00l$ 2_1 $c'-$		$hk0$ a *G* $00l$ 2_1 *S*		$h0l$ c *G*
66	$C\,2/c\,2/c\,2/m$	$00l$ c $c'-$	$00l$ c $c'-$			$0kl$ c *G*	$h0l$ c *G*
67	$C\,2/m\,2/m\,2/a$				$hk0$ a *G*		

Table 2.5.3.5. *Conditions for observation of GS bands for the 137 space groups exhibiting these extinctions* (*cont.*)

Space group		Incident-beam direction											
		[100]		[010]		[001]		[*uv*0]		[0*vw*]		[*u*0*w*]	
68	*C* 2/*c* 2/*c* 2/*a*	00*l* *c*	*c*′–	00*l* *c*	*c*′–			*hk*0 *a*	*G*	0*kl* *c*	*G*	*h*0*l* *c*	*G*
70	*F* 2/*d* 2/*d* 2/*d*	00*l*, 0*k*0 *d*	*d*′–	*h*00, 00*l* *d*	*d*′–	0*k*0, *h*00 *d*	*d*′–	*hk*0 *d*	*G*	0*kl* *d*	*G*	*h*0*l* *d*	*G*
72	*I* 2/*b* 2/*a* 2/*m*		*b*′–		*a*′–					0*kl* *b*	*G*	*h*0*l* *a*	*G*
73	*I* 2/*b* 2/*c* 2/*a*		*b*′–		*c*′–		*a*′–	*hk*0 *a*	*G*	0*kl* *b*	*G*	*h*0*l* *c*	*G*
74	*I* 2/*m* 2/*m* 2/*a*							*hk*0 *a*	*G*				

Point groups 4, $\bar{4}$, 4/*m*

Space group		Incident-beam direction	
		[*uv0*]	
76	$P4_1$	00*l* 4_1	*S*
78	$P4_3$	00*l* 4_3	*S*
85	$P4/n$	*hk*0 *n*	*G*
86	$P4_2/n$	*hk*0 *n*	*G*
88	$I4_1/a$	*hk*0 *a*	*G*

Point group 422

Space group		Incident-beam direction			
		[*uv0*]		[0*vw*]	
90	$P42_12$			*h*00 2_1	*S*
91	$P4_122$	00*l* 4_1	*S*		
92	$P4_12_12$	00*l* 4_1	*S*	*h*00 2_1	*S*
94	$P4_22_12$			*h*00 2_1	*S*
95	$P4_322$	00*l* 4_3	*S*		
96	$P4_32_12$	00*l* 4_3	*S*	*h*00 2_1	*S*

Point group 4*mm*

Space group		Incident-beam direction									
		[100]		[001]		[110]		[*u*0*w*] and [0*vw*]*		[*uūw*]	
100	*P*4*bm*			*h*00, 0*k*0 *a* *b*	*G*			*h*0*l*, 0*kl* *a* *b*	*G*		
101	$P4_2cm$	00*l* *c*	*c*′–					*h*0*l*, 0*kl* *c*	*G*		
102	$P4_2nm$	00*l* *n*	*n*′–	*h*00, 0*k*0 *n*	*G*			*h*0*l*, 0*kl* *n*	*G*		
103	*P*4*cc*	00*l* *c*	*c*′–			00*l* *c*	*c*′–	*h*0*l*, 0*kl* *c*	*G*	*hhl* *c*	*G*
104	*P*4*nc*	00*l* *n*	*n*′–	*h*00, 0*k*0 *n*	*G*	00*l* *c*	*c*′–	*h*0*l*, 0*kl* *n*	*G*	*hhl* *c*	*G*
105	$P4_2mc$					00*l* *c*	*c*′–			*hhl* *c*	*G*

Table 2.5.3.5. *Conditions for observation of GS bands for the 137 space groups exhibiting these extinctions* (*cont.*)

Space group	Incident-beam direction				
	[100]	[001]	[110]	[*u*0*w*] and [0*vw*]*	[*uūw*]
106 $P4_2bc$		*h*00, 0*k*0 *a* *b* *G*	00*l* *c* *c*′−	*h*0*l*, 0*kl* *a* *b* *G*	*hhl* *c* *G*
108 $I4cm$				*h*0*l*, 0*kl* *c* *G*	
109 $I3_1md$		*hh*0 $\bar{h}h$0 *G* *d*	00*l* *d* *d*′−		*hhl* *G* *d*
110 $I4_1cd$		*hh*0 $\bar{h}h$0 *G* *d*	00*l* *d* *d*′−	*h*0*l*, 0*kl* *G* *c*	*hhl* *G* *d*

* Conditions in this column are cyclic on *h* and *k*.

Point groups $\bar{4}2m$, 4/*mmm*

Space group	Incident-beam direction					
	[100]	[001]	[110]	[*u*0*w*] and [0*vw*]*	[*uuw*]	[*uv*0]
112 $P\bar{4}2c$			00*l* *c* *c*′−		*hhl* *c* *G*	
113 $P\bar{4}2_1m$	0*k*0 2_1 *S*	*h*00, 0*k*0 2_1 *S*		0*k*0, *h*00 2_1 *S*		
114 $P\bar{4}2_1c$	0*k*0 2_1 *S*	*h*00, 0*k*0 2_1 *S*	00*l* *c* *c*′−	0*k*0, *h*00 2_1 *S*	*hhl* *c* *G*	
116 $P\bar{4}c2$	00*l* *c* *c*′−			*h*0*l*, 0*kl* *c* *G*		
117 $P\bar{4}b2$		*h*00, 0*k*0 *a* *b* *G*		*h*0*l*, 0*kl* *a* *b* *G*		
118 $P\bar{4}n2$	00*l* *n* *n*′−	*h*00, 0*k*0 *n* *G*		*h*0*l*, 0*kl* *n* *G*		
120 $I\bar{4}c2$				*h*0*l*, 0*kl* *c* *G*		
122 $I\bar{4}2d$		*hh*0 $\bar{h}h$0 *G* *d*	00*l* *d* *d*′−		*hhl* *G* *d*	
124 $P\,4/m\,2/c\,2/c$	00*l* *c* *c*′−		00*l* *c* *c*′−	*h*0*l*, 0*kl* *c* *G*	*hhl* *c* *G*	
125 $P\,4/n\,2/b\,2/m$	0*k*0 *n* *b*′−	*h*00, 0*k*0 *a* *b* *n*′−		*h*0*l*, 0*kl* *a* *b* *G*		*hk*0 *n* *G*
126 $P\,4/n\,2/n\,2/c$	0*k*0 *n* 00*l* *n* *n*′−	*h*00, 0*k*0 *n* *n*′−	00*l* *c* *c*′−	*h*0*l*, 0*kl* *n* *G*	*hhl* *c* *G*	*hk*0 *n* *G*
127 $P\,4/m\,2_1/b\,2/m$	0*k*0 2_1 *b*′−	*h*00 $a+2_1$ *GS* 0*k*0 $b+2_1$		*h*0*l*, 0*kl* *a* *b* *G* 0*k*0, *h*00 2_1 *S*		

Table 2.5.3.5. *Conditions for observation of GS bands for the 137 space groups exhibiting these extinctions* (*cont.*)

Space group		Incident-beam direction					
		[100]	[001]	[110]	[$u0w$] and [$0vw$]*	[uuw]	[$uv0$]
128	$P\,4/m\,2_1/n\,2/c$	$00l$, $0k0$ n 2_1 $n'-$	$h00$, $0k0$ $n+2_1$ *GS*	$00l$ c $c'-$	$h0l$, $0kl$ n *G* $0k0$, $h00$ 2_1 *S*	hhl c *G*	
129	$P\,4/n\,2_1/m\,2/m$	$0k0$ $n+2_1$ *GS*	$h00$, $0k0$ 2_1 $n'-$		$0k0$, $h00$ 2_1 *S*		$hk0$ n *G*
130	$P\,4/n\,2_1/c\,2/c$	$0k0$ $n+2_1$ *GS* $00l$ c $c'-$	$h00$, $0k0$ 2_1 $n'-$	$00l$ c $c'-$	$h0l$, $0kl$ c *G* $0k0$, $h00$ 2_1 *S*	hhl c *G*	$hk0$ n *G*
131	$P\,4_2/m\,2/m\,2/c$			$00l$ c $c-$		hhl c *G*	
132	$P\,4_2/m\,2/c\,2/m$	$00l$ c $c'-$			$h0l$, $0kl$ c *G*		
133	$P\,4_2/n\,2/b\,2/c$	$0k0$ n $b'-$	$h00$, $0k0$ a b $n'-$	$00l$ c $c'-$	$h0l$, $0kl$ a b *G*	hhl c *G*	$hk0$ n *G*
134	$P\,4_2/n\,2/n\,2/m$	$0k0$, $00l$ n $n'-$	$h00$, $0k0$ n $n'-$		$h0l$, $0kl$ n *G*		$hk0$ n *G*
135	$P\,4_2/m\,2_1/b\,2/c$	$0k0$ 2_1 $b'-$	$h00$, $0k0$ $a+2_1$ $b+2_1$ *GS*	$00l$ c $c'-$	$h0l$, $0kl$ a b *G* $0k0$, $h00$ 2_1 *S*	hhl c *G*	
136	$P\,4_2/m\,2_1/n\,2/m$	$00l$, $0k0$ n 2 $n'-$	$h00$, $0k0$ $n+2_1$ *GS*		$h0l$, $0kl$ n *G* $0k0$, $h00$ 2_1 *S*		
137	$P\,4_2/n\,2_1/m\,2/c$	$0k0$ $n+2_1$ *GS*	$h00$, $0k0$ 2_1 $n'-$	$00l$ c $c'-$	$0k0$, $h00$ 2_1 *S*	hhl c *G*	$hk0$ n *G*
138	$P\,4_2/n\,2_1/c\,2/m$	$0k0$ $n+2_1$ *GS* $00l$ c $c'-$	$h00$, $0k0$ 2_1 $n'-$		$h0l$, $0kl$ c *G* $0k0$, $h00$ 2_1 *S*		$hk0$ n *G*
140	$I\,4/m\,2/c\,2/m$				$h0l$, $0kl$ c *G*		
141	$I\,4_1/a\,2/m\,2/d$		$hh0$ $\bar{h}h0$ d $a'-$	$00l$, $\bar{h}h0$ d a $d'-$		hhl d *G*	$hk0$ a *G*
142	$I\,4_1/a\,2/c\,2/d$		$hh0$ $\bar{h}h0$ d $a'-$	$00l$, $\bar{h}h0$ d a $d'-$	$h0l$, $0kl$ c *G*	hhl d *G*	$hk0$ a *G*

* Conditions in this column are cyclic on h and k.

Table 2.5.3.5. *Conditions for observation of GS bands for the 137 space groups exhibiting these extinctions* (*cont.*)

Point groups 3*m*, $\bar{3}m$, 6, 6/*m*, 622, 6*mm*, $\bar{6}m2$, 6/*mmm*

Space group		Incident-beam direction			
		[100]	[210]	[2*u u w*]	[*v*0*w*]
158	$P3c1$		$000l$ c G	$hh2\bar{h}l$ c G	
159	$P31c$	$000l$ c G			$h\bar{h}0l$ c G
161	$R3c$		$000l$ $l = 6n + 3$ G c	$hh2\bar{h}l$ G c	
163	$P\bar{3}1c$	$000l$ c G			$h\bar{h}0l$ c G
165	$P\bar{3}c1$		$000l$ c G	$hh2\bar{h}l$ c G	
167	$R\bar{3}c$		$000l$ $l = 6n + 3$ G c	$hh2\bar{h}l$ G c	
169	$P6_1$	$000l$ 6_1 S	$000l$ 6_1 S		
170	$P6_5$	$00l$ 6_5 S	$00l$ 6_5 S		
173	$P6_3$	$000l$ 6_3 S	$000l$ 6_3 S		
176	$P6_3/m$	$000l$ 6_3 S	$000l$ 6_3 S		
178	$P6_122$	$000l$ 6_1 S	$000l$ 6_1 S		
179	$P6_522$	$000l$ 6_5 S	$000l$ 6_5 S		
182	$P6_322$	$000l$ 6_3 S	$000l$ 6_3 S		
184	$P6cc$	$000l$ c $c'-$	$000l$ c $c'-$	$hh2\bar{h}l$ c G	$h\bar{h}0l$ c G
185	$P6_3cm$	$000l$ 6_3 $c'-$	$000l$ $c + 6_3$ GS	$hh2\bar{h}l$ c G	
186	$P6_3mc$	$000l$ $c + 6_3$ GS	$000l$ 6_3 $c'-$		$h\bar{h}0l$ c G
188	$P\bar{6}c2$		$000l$ c G	$hh2\bar{h}l$ c G	
190	$P\bar{6}c2$	$000l$ c G			$h\bar{h}0l$ c G
192	$P6/mcc$	$000l$ c $c'-$	$000l$ c $c'-$	$hh2\bar{h}l$ c G	$h\bar{h}0l$ c G
193	$P6_3/mcm$	$00l$ 6_3 $c'-$	$000l$ $c + 6_3$ GS	$hh2\bar{h}l$ c G	
194	$P6_3/mmc$	$000l$ $c + 6_3$ GS	$000l$ 6_3 $c'-$		$h\bar{h}0l$ c G

Table 2.5.3.5. *Conditions for observation of GS bands for the 137 space groups exhibiting these extinctions* (*cont.*)

Point groups 23, *m*3, 432, *m*3*m*

Space group		Incident-beam direction			
		[100] (cyclic)	[110] (cyclic)	[*uv*0] (cyclic)	[*uuw*] (cyclic)
198	$P2_13$	$00l$, $0k0$ 2_1 S	$00l$ 2_1 S	$00l$ 2_1 S	
201	$Pn\bar{3}$ $P2/n\bar{3}$	$00l$, $0k0$ n $n'-$		$\bar{k}h0$ n G	
203	$Pd\bar{3}$ $F2/d\bar{3}$	$00l$, $0k0$ d $d'-$		$\bar{k}h0$ d G	
205	$Pa\bar{3}$ $P2_1/a\bar{3}$	$00l$ $c+2_1$ GS $0k0$ 2_1 $b'-$	$00l$ 2_1 S $\bar{h}h0$ a G	$00l$ 2_1 S $\bar{k}h0$ a G	
206	$Ia\bar{3}$ $I2_1/a\bar{3}$		$\bar{h}h0$ a G	$\bar{k}h0$ a G	
212	$P4_332$			$00l$ 4_3 S	
213	$P4_132$			$00l$ 4_1 S	
218	$P\bar{4}3n$		$00l$ c $n-$	hhl c G	
219	$F\bar{4}3c$			hhl c G	
220	$I\bar{4}3d$	$0kk$ $0\bar{k}k$ d G	$00l$ d $d-$	hhl d G	
222	$Pn\bar{3}n$	$00l$, $0k0$ n $n'-$	$00l$ c $n-$	$hk0$ n G	hhl c G
223	$Pm\bar{3}n$		$00l$ c $n'-$		hhl c G
224	$Pn\bar{3}m$	$00l$, $0k0$ n $n'-$		$hk0$ n G	
226	$Fm\bar{3}c$				hhl c G
227	$Fd\bar{3}m$	$00l$, $0k0$ d $d'-$		$hk0$ d G	
228	$Fd\bar{3}c$	$00l$, $0k0$ d $d'-$		$hk0$ d G	hhl c G
230	$Ia\bar{3}d$	$0kk$ $0\bar{k}k$ d $b'-$	$00l$, $\bar{h}h0$ $d\quad a$ $d'-$	$hk0$ a G	hhl d G

patterns]. Contact J. M. Zuo or J. C. H. Spence, Physics Department, Arizona State University, Tempe, Arizona, USA.

(2) A package for CBED pattern simulation by both Bloch-wave and multi-slice methods is available from P. Stadelmann (pierre.stadelmann@cime.uhd.edfl.ch), Lausanne, Switzerland, in UNIX for workstations [Silicon Graphics, Dec Alpha (OSF), IBM RISC 6000, SUN and HP-9000].

(3) HOLZ line simulations: Listing for PC 8801 (NEC): Tanaka & Terauchi (1985, pp. 174–175).

2.5.4. Electron-diffraction structure analysis (EDSA)

(B. K. VAINSHTEIN AND B. B. ZVYAGIN)

2.5.4.1. *Introduction*

Electron-diffraction structure analysis (EDSA) (Vainshtein, 1964) based on electron diffraction (Pinsker, 1953) is used for the investigation of the atomic structure of matter together with X-ray and neutron diffraction analysis. The peculiarities of EDSA, as compared with X-ray structure analysis, are defined by a strong interaction of electrons with the substance and by a short wavelength λ. According to the Schrödinger equation (see Section 5.2.2) the electrons are scattered by the electrostatic field of an object. The values of the atomic scattering amplitudes, f_e, are three orders higher than those of X-rays, f_x, and neutrons, f_n. Therefore, a very small quantity of a substance is sufficient to obtain a diffraction pattern. EDSA is used for the investigation of very thin single-crystal films, of ~5–50 nm polycrystalline and textured films, and of deposits of finely grained materials and surface layers of bulk specimens. The structures of many ionic crystals, crystal hydrates and hydro-oxides, various inorganic, organic, semiconducting and metallo-organic compounds, of various minerals, especially layer silicates, and of biological structures have been investigated by means of EDSA; it has also been used in the study of polymers, amorphous solids and liquids.

Special areas of EDSA application are: determination of unit cells; establishing orientational and other geometrical relationships between related crystalline phases; phase analysis on the basis of d_{hkl} and I_{hkl} sets; analysis of the distribution of crystallite dimensions in a specimen and inner strains in crystallites as determined from line profiles; investigation of the surface structure of single crystals; structure analysis of crystals, including atomic position determination; precise determination of lattice potential distribution and chemical bonds between atoms; and investigation of crystals of biological origin in combination with electron microscopy (Vainshtein, 1964; Pinsker, 1953; Zvyagin, 1967; Pinsker *et al.*, 1981; Dorset, 1976; Zvyagin *et al.*, 1979).

There are different kinds of electron diffraction (ED) depending on the experimental conditions: high-energy (HEED) (above 30–200 kV), low-energy (LEED) (10–600 V), transmission (THEED), and reflection (RHEED). In electron-diffraction studies use is made of special apparatus – electron-diffraction cameras in which the lens system located between the electron source and the specimen forms the primary electron beam, and the diffracted beams reach the detector without aberration distortions. In this case, high-resolution electron diffraction (HRED) is obtained. ED patterns may also be observed in electron microscopes by a selected-area method (SAD). Other types of electron diffraction are: MBD (microbeam), HDD (high-dispersion), CBD (convergent-beam), SMBD (scanning-beam) and RMBD (rocking-beam) diffraction (see Sections 2.5.2 and 2.5.3). The recent development of electron diffractometry, based on direct intensity registration and measurement by scanning the diffraction pattern against a fixed detector (scintillator followed by photomultiplier), presents a new improved level of EDSA which provides higher precision and reliability of structural data (Avilov *et al.*, 1999; Tsipursky & Drits, 1977; Zhukhlistov *et al.*, 1997, 1998; Zvyagin *et al.*, 1996).

Electron-diffraction studies of the structure of molecules in vapours and gases is a large special field of research (Vilkov *et al.*, 1978). See also *Stereochemical Applications of Gas-Phase Electron Diffraction* (1988).

2.5.4.2. *The geometry of ED patterns*

In HEED, the electron wavelength λ is about 0.05 Å or less. The Ewald sphere with radius λ^{-1} has a very small curvature and is approximated by a plane. The ED patterns are, therefore, considered as plane cross sections of the reciprocal lattice (RL) passing normal to the incident beam through the point 000, to scale $L\lambda$ (Fig. 2.5.4.1). The basic formula is

$$r = |\mathbf{h}|L\lambda, \text{ or } rd = L\lambda, \qquad (2.5.4.1)$$

where r is the distance from the pattern centre to the reflection, $\mathbf{h}$ is the reciprocal-space vector, d is the appropriate interplanar distance and L is the specimen-to-screen distance. The deviation of the Ewald sphere from a plane at distance h from the origin of the coordinates is $\delta_h = h^2\lambda/2$. Owing to the small values of λ and to the rapid decrease of f_e depending on $(\sin\theta)/\lambda$, the diffracted beams are concentrated in a small angular interval (≤ 0.1 rad).

Single-crystal ED patterns image one plane of the RL. They can be obtained from thin ideal crystalline plates, mosaic single-crystal films, or, in the RHEED case, from the faces of bulk single crystals. Point ED patterns can be obtained more easily owing to the following factors: the small size of the crystals (increase in the dimension of RL nodes) and mosaicity – the small spread of crystallite orientations in a specimen (tangential tension of the RL nodes). The crystal system, the parameters of the unit cell and the Laue symmetry are determined from point ED patterns; the probable space group is found from extinctions. Point ED patterns may be used for intensity measurements if the kinematic approximation holds true or if the contributions of the dynamic and secondary scattering are not too large.

The indexing of reflections and the unit-cell determination are carried out according to the formulae relating the RL to the DL (direct lattice) (Vainshtein, 1964; Pinsker, 1953; Zvyagin, 1967).

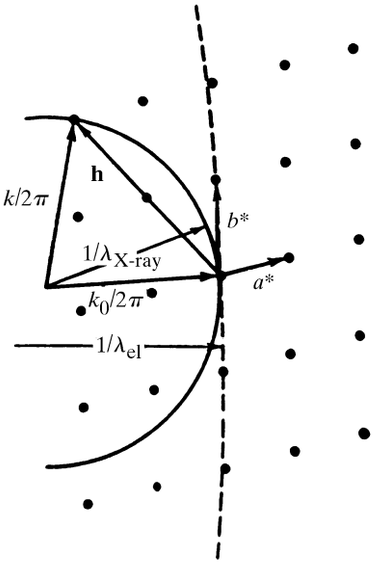

Fig. 2.5.4.1. Ewald spheres in reciprocal space. Dotted line: electrons, solid line: X-rays.

references